Journal of Physics G: Nuclear and Particle Physics

PAPER

# Revealing the structure of light pseudoscalar mesons at the electron–ion collider

To cite this article: J Arrington *et al* 2021 *J. Phys. G: Nucl. Part. Phys.* **48** 075106

IOP Publishing
Journal of Physics G: Nuclear and Particle Physics
J. Phys. G: Nucl. Part. Phys. **48** (2021) 075106 (47pp)
https://doi.org/10.1088/1361-6471/abf5c3

# Revealing the structure of light pseudoscalar mesons at the electron–ion collider

**J Arrington[1], C Ayerbe Gayoso[2], P C Barry[3,4], V Berdnikov[5], D Binosi[6], L Chang[7], M Diefenthaler[3], M Ding[6], R Ent[3], T Frederico[8], Y Furletova[3], T J Hobbs[3,9,10], T Horn[3,5,*], G M Huber[11], S J D Kay[11], C Keppel[3], H-W Lin[12], C Mezrag[13], R Montgomery[14], I L Pegg[5], K Raya[7,15], P Reimer[16], D G Richards[3], C D Roberts[17,18], J Rodríguez-Quintero[19], D Romanov[3], G Salmè[20], N Sato[3], J Segovia[21], P Stepanov[5], A S Tadepalli[3] and R L Trotta[5]**

[1] Lawrence Berkeley National Laboratory, Berkeley, CA 94720, United States of America
[2] Mississippi State University, Starkville, MS, United States of America
[3] Thomas Jefferson National Accelerator Facility, Newport News, VA 23606, United States of America
[4] North Carolina State University, Raleigh, NC 27607, United States of America
[5] Catholic University of America, Washington, DC, United States of America
[6] European Centre for Theoretical Studies in Nuclear Physics and Related Areas (ECT*) and Fondazione Bruno Kessler Villa Tambosi, Strada delle Tabarelle 286, I-38123 Villazzano (TN) Italy
[7] School of Physics, Nankai University, Tianjin 300071, People's Republic of China
[8] Instituto Tecnológico de Aeronáutica, 12.228-900 São José dos Campos, Brazil
[9] Southern Methodist University, Dallas, TX 75275-0175, United States of America
[10] Department of Physics, Illinois Institute of Technology, Chicago, IL 60616, United States of America
[11] University of Regina, Regina, SK S4S 0A2, Canada
[12] Michigan State University, East Lansing, MI 48824, United States of America
[13] IRFU, CEA, Université Paris-Saclay, F-91191 Gif-sur-Yvette, France
[14] SUPA School of Physics and Astronomy, University of Glasgow, Glasgow G12 8QQ, United Kingdom
[15] Instituto de Ciencias Nucleares, Universidad Nacional Autónoma de México, Apartado Postal 70-543, C.P. 04510, CDMX, Mexico
[16] Argonne National Laboratory, Lemont, IL 60439, United States of America
[17] School of Physics, Nanjing University, Nanjing, Jiangsu 210093, People's Republic of China

---

[*] Author to whom any correspondence should be addressed.

0954-3899/21/075106+47$33.00

[18] Institute for Nonperturbative Physics, Nanjing University, Nanjing, Jiangsu 210093, People's Republic of China
[19] Department of Integrated Sciences and Center for Advanced Studies in Physics, Mathematics and Computation, University of Huelva, E-21071 Huelva, Spain
[20] Istituto Nazionale di Fisica Nucleare, Sezione di Roma, P.le A. Moro 2, I-00185 Rome, Italy
[21] Departamento de Sistemas Físicos, Químicos y Naturales, Universidad Pablo de Olavide, E-41013 Sevilla, Spain

E-mail: hornt@cua.edu

Received 21 February 2021, revised 19 March 2021
Accepted for publication 7 April 2021
Published 25 May 2021

## Abstract

The questions of how the bulk of the Universe's visible mass emerges and how it is manifest in the existence and properties of hadrons are profound, and probe the heart of strongly interacting matter. Paradoxically, the lightest pseudoscalar mesons appear to be key to a further understanding of the emergent mass and structure mechanisms. These mesons, namely, the pion and kaon, are the Nambu–Goldstone boson modes of quantum chromodynamics (QCD). Unravelling their partonic structure and the interplay between emergent and Higgs-boson mass mechanisms is a common goal of three interdependent approaches—continuum QCD phenomenology, lattice-regularised QCD, and the global analysis of parton distributions—linked to experimental measurements of hadron structure. Experimentally, the anticipated electron–ion collider will enable a revolution in our ability to study pion and kaon structures, accessed by scattering from the 'meson cloud' of the proton through the Sullivan process. With the goal of enabling a suite of measurements that can address these questions, we examine key reactions that identify the critical detector-system requirements needed to map tagged pion and kaon cross-sections over a wide range of kinematics. The excellent prospects for extracting pion structural, functional, and form-factor data are outlined, and similar prospects for kaon structures are discussed in the context of a worldwide programme. The successful completion of the programme outlined herein will deliver deep, far-reaching insights into the emergence of pions and kaons, their properties, and their role as QCD's Goldstone boson modes.

Keywords: electron–ion collider, electromagnetic form factors—elastic and transition, emergence of mass, Nambu–Goldstone modes—pions and kaons, parton distributions, strong interactions in the standard model of particle physics, hadron structure

(Some figures may appear in colour only in the online journal)

## 1. Introduction

### *1.1. Mass budgets*

The Standard Model has two mechanisms for mass generation. One is connected with the Higgs boson (HB) [1], discovered at the Large Hadron Collider in 2012 [2, 3]. In the context of strong interactions, the Higgs boson produces the Lagrangian current-mass for each of the quarks. Yet, regarding the kernels of all known nuclei, these current masses account for less than 2% of the mass of a neutron or proton. More than 98% of the visible mass emerges as a consequence of strong interactions within Quantum ChromoDynamics (QCD) [4–6]: this is Emergent Hadronic Mass (EHM).

Consider, therefore, the Lagrangian of QCD in the absence of Higgs couplings to the quarks. Classically, it defines a scale-invariant theory; and scale-invariant theories do not support dynamics. Therefore, bound states are impossible and the Universe cannot exist.

The process of renormalisation in the quantisation of chromodynamics introduces a mass which breaks the scale invariance of classical theory. Hence, in the absence of quark couplings to the HB, i.e. in the chiral limit, the QCD stress–energy tensor, $T_{\mu\nu}$, exhibits a trace anomaly [7]:

$$T_{\mu\mu} = \beta(\alpha(\zeta))\frac{1}{4}G^a_{\mu\nu}G^a_{\mu\nu} =: \Theta_0, \tag{1}$$

where $\beta(\alpha(\zeta))$ is QCD's $\beta$-function, $\alpha(\zeta)$ is the associated running coupling, $G^a_{\mu\nu}$ is the gluon field's strength tensor, and $\zeta$ is the renormalisation scale. The consequences of equation (1) are wide-ranging, with strong impacts.

A first question to ask is whether the magnitude of $\Theta_0$ can be measured and understood. Measurement is straightforward. Consider the following in-proton expectation value:

$$\langle p(P)|T_{\mu\nu}|p(P)\rangle = -P_\mu P_\nu, \tag{2}$$

where the equations of motion for a one-particle proton state produce the right-hand side. In the chiral limit

$$\langle p(P)|T_{\mu\mu}|p(P)\rangle = -P^2 = m_p^2 = \langle p(P)|\Theta_0|p(P)\rangle. \tag{3}$$

As highlighted by the blue domain in figure 1(A), this expectation value is 94% of the proton's measured mass. Since $\Theta_0$ is expressed solely in terms of gluons when a (large-$\zeta$) parton basis is used, one might then conclude that the chiral-limit value of $m_p$ is generated completely by glue.

However complex that might seem, Nature is even more subtle. This may be seen by returning to equation (2) and replacing the proton by the pion;

$$\langle \pi(q)|T_{\mu\nu}|\pi(q)\rangle = -q_\mu q_\nu \Rightarrow \langle \pi(q)|\Theta_0|\pi(q)\rangle = m_\pi^2 \overset{\text{chiral limit}}{=} 0 \tag{4}$$

because the chiral-limit pion is a massless Nambu–Goldstone (NG) mode [10, 11]. This feature is highlighted by the complete absence of a blue domain for the pion in figure 1(C). Conceivably, this could mean that the scale anomaly is trivially zero in the pion; to wit, strong gluon–gluon interactions have no effect in the pion because each term required to express $\Theta_0$ vanishes separately [12]. However, such an explanation would sit uncomfortably with known QCD dynamics, which expresses both attraction and repulsion, and often remarkable fine tuning, but never inactivity. (An additional discussion of these points may be found, e.g., in [4], section V], [5], sections 4.4 and 4.5]).

Switching on the HB couplings to light quarks, one then encounters the other two wedges in figure 1(A): the grey area shows the sum of Higgs-generated valence-quark current-masses in the proton, which amounts to just $0.01 \times m_p$; and orange indicates the contribution generated by constructive interference between the EHM and HB effects, 5%. Again, the picture for the pion is completely different: EHM + HB interference is responsible for 95% of the pion's mass. The kaon lies somewhere between these extremes. It is a would-be NG mode, so there is

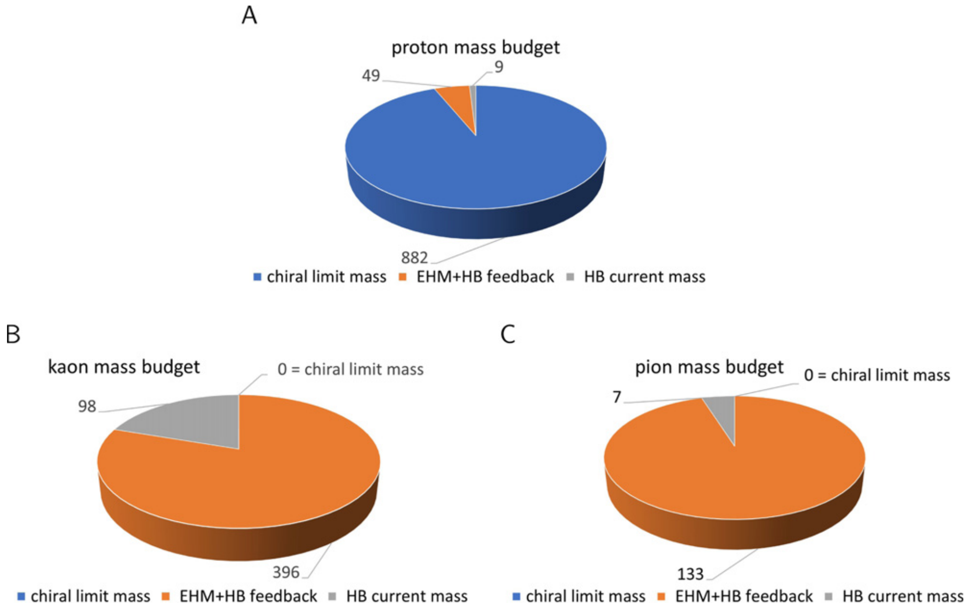

**Figure 1.** Mass budgets for the proton (A), kaon (B), and pion (C). The differences are stark. Due to EHM, the proton's mass is large in the chiral limit. Conversely, and yet still owing to EHM via its corollary, dynamic chiral symmetry breaking (DCSB), the kaon and pion are massless in the absence of quark couplings to the HB. (Units MeV, Poincaré-invariant separation at $\zeta = 2$ GeV, breakdowns produced using information from [8, 9].) Reproduced from [6]. CC BY 4.0.

no blue domain in figure 1(B); but the sum of the valence-quark and valence-antiquark current masses in the kaon amounts to 20% of its measured mass—four times more than in the pion, and EHM + HB interference produce 80%.

Equations (3), (4), and the mass budgets drawn in figure 1 demand interpretation. They stress that any explanation of the proton's mass is incomplete unless it simultaneously clarifies equation (4). Moreover, both phenomena are coupled with confinement, which is fundamental to the proton's stability. These remarks highlight the ubiquitous influence of EHM. They emphasise that in order to finally complete the Standard Model, it is crucial to understand the emergence of mass within the strong interaction and the modulating effects of HB mass generation, both of which are fundamental to understanding the evolution of our Universe.

In facing these questions, unique insights can be obtained by focussing on the properties of QCD's (pseudo-) NG modes, i.e. pions and kaons; diverse phenomenological and theoretical approaches are now being deployed in order to develop a coherent image of these bound states. Complete understanding demands that tight links be drawn between dynamics in QCD's gauge sector and pion and kaon light-front wave functions, and from there to observables, such as pion and kaon elastic form factors and distribution amplitudes (DAs) and functions. Herein, we propose an array of measurements and associated analyses designed to deliver significant progress towards these goals [13, 14].

It is worth remarking here that *measurements* of form factors, DAs and functions, spectra, charge radii, etc., are all on the same footing. Theory supplies predictions for such quantities. Experiments measure precise cross-sections; and cross-sections are expressed, via truncations that optimally have the quality of approximations, in terms of the desired quantity.

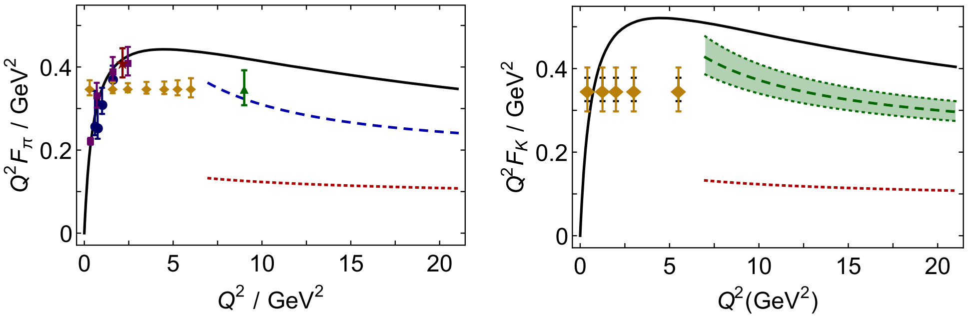

**Figure 2.** The left (right) panel shows calculations, measurements, and the projected precision of future measurements of $Q^2F_\pi(Q^2)$ $(Q^2F_K(Q^2))$. Solid curve—prediction from [36, 37]; dotted curve—result produced by the hard-scattering formula, equation (5), using the asymptotic DA; dashed curve—result produced by the hard-scattering formula using the DA calculated in the CSM framework at a scale relevant to the experiment. Stars [39], circles, and squares [40] represent existing data; diamonds and triangles show the anticipated reach and accuracy of forthcoming experiments [41–43]. (left) Adapted figure with permission from [38], Copyright 2017 by the American Physical Society.

At question is the reliability of the truncation/approximation employed in relating the measured cross-section to this quantity. The phenomenology challenge is to ensure that every contribution known to have a material effect is included in building the bridge. The quality of the phenomenology can alter neither that of the experiment nor the theory. However, inadequate phenomenology can deliver results that mislead interpretation. The reverse is also true. Thus, progress requires the construction of a positive synergy between all subbranches of the programme.

### *1.2. EIC context*

The electron–ion collider (EIC) [15] will be capable of addressing an array of profound questions that probe the heart and reach out to the frontiers of strong interactions within the Standard Model. Looming large in this array are the emergence of the bulk of visible mass and its manifestations in the existence and properties of hadrons and nuclei. The research described herein aims to build a path towards answers by focussing on the properties of pions and kaons, the Standard Model's would-be NG modes. It combines experiment, phenomenology and theory in a synergistic effort to reveal: how the roughly 1 GeV mass-scale that characterises atomic nuclei appears; why it has the observed value; why ground-state pseudoscalar mesons are unnaturally light in comparison; and the role of the HB in forming hadron properties.

The focus on pions and kaons acknowledges that these states are unique expressions of Standard Model dynamics that exhibit a peculiar dichotomy. Namely, they are hadron bound states, defined, like all others, by their valence quark and/or antiquark content, making the calculation of their properties no different, in principle, from proton computations; but the mechanism(s) which give all other hadrons their roughly 1 GeV mass-scale are obscured in these systems. This elevates studies of the pion and kaon structures to the highest levels of importance. Yet, although discovered more than seventy years ago [16, 17], remarkably little is known about their structure. The EIC, with its high luminosity and wide kinematic range, offers an extraordinary new opportunity to eliminate that ignorance. There is much to be learnt: pions and kaons are not pointlike; their internal structure is more complex than is usually imagined; and the properties of these nearly-massless strong-interaction composites provide the clearest windows onto EHM and its modulation by HB interactions.

This report identifies a raft of measurements and associated phenomenology and theory that will exploit the distinctive strengths of the EIC in driving towards answers to some of the most basic questions in Nature. The successful completion of the programme will deliver deep, far-reaching insights into the distributions and apportionment of mass and spin within the pion and kaon; the similarities and differences between such distributions in these (almost) NG modes and the benchmark proton; the symbiotic relationship between EHM and confinement; and the character and consequences of constructive interference between the Standard Model's two mass-generating mechanisms.

## 2. Meson structure as a QCD laboratory—status and prospects

### 2.1. Pion and kaon structure—theoretical status

EHM is an elemental feature of the Standard Model. As reviewed elsewhere [4–6, 18], it is the origin of a running gluon mass, the source of DCSB, and very probably crucial to any explanation of confinement. DCSB is basic to understanding the notion of constituent quarks and the successes of related models; and it provides the foundation for the existence of nearly-massless pseudo-Goldstone modes. Confinement is related to the empirical fact that all attempts to remove a single quark or gluon from within a hadron and isolate it in a detector have failed. The mechanisms responsible for EHM must not only be expressed in hadron masses, but in their wave functions, with the associated Fock-space representation in terms of quarks and gluons; and, in particular, in the corresponding light-hadron structural observables. In the following, examples of such measurable quantities will be presented, focussed largely on pion and kaon observables accessible at the EIC. The kaon is very interesting because competition between emergent and Higgs-driven mass generation takes place within it. All the differences between the pion and kaon are driven by the Higgs-induced modulation of EHM.

*2.1.1. Pion and kaon distribution amplitudes.* The cross-sections of many hard exclusive hadronic reactions can be expressed in terms of the parton DAs of the hadrons involved. For instance, in the case of the electromagnetic form factor of light pseudoscalar mesons [19–22]:

$$\exists Q_0 > \Lambda_{\mathrm{QCD}} | Q^2 F_{\mathrm{P}}(Q^2) \overset{Q^2>Q_0^2}{\approx} 16\pi\alpha_{\mathrm{s}}(Q^2) f_{\mathrm{P}}^2 w_\varphi^2 \,,$$

with

$$w_\varphi = \frac{1}{3}\int_0^1 \mathrm{d}x \, \frac{1}{x} \, \varphi_{\mathrm{P}}(x), \tag{5}$$

where $\alpha_{\mathrm{s}}(Q^2)$ is the strong running coupling, $f_{\mathrm{P}}$ is the pseudoscalar meson's leptonic decay constant and $\varphi_{\mathrm{P}}(x)$ is the DA of the pseudoscalar meson. However, the value of $Q_0$ is not predicted by QCD and the DAs are not determined by the analysis framework; perturbative QCD (pQCD) only states that $\varphi_{\mathrm{P}}(x) \approx \varphi_{\mathrm{as}}(x) = 6x(1-x)$ for $Q^2 \gg Q_0^2$.

One may alternatively use continuum Schwinger function methods (CSMs) for QCD to describe exclusive reactions in terms of Poincaré-covariant hadron bound-state amplitudes (BSAs). This approach has been formulated in both Euclidean [23–27] and Minkowski [28–33] spaces. Moreover, recent progress within CSMs has established that the hadron DA, which is essentially nonperturbative, can be obtained as a light-front projection of the hadron's

BSA [34], an approach first employed in [35]. Using this connection, the solid curves of figure 2 are the CSM's predictions for the pion [36, 37] and kaon [38] elastic electromagnetic form factors to arbitrarily large $Q^2$. Also depicted (dashed curves) are the results obtained using equation (5) and the DAs calculated in the CSM framework at a scale relevant to the experiment. These DAs are very different from $\varphi_{\rm as}(x)$, being markedly broader owing to EHM. The dotted curve in both panels is the hard scattering formula, equation (5), computed with the asymptotic profile, $\varphi_{\rm as}(x)$.

With the continuing development of Euclidean and Minkowski space approaches using the CSM framework, it will become possible to provide an estimate for $Q_0$ in equation (5) by comparing the full covariant form factor with the valence one, which should dominate at large momenta. Here, the differences between the results serve to quantify the contribution from higher Fock components of the light-front wave function to the pion charge distribution.

As remarked above and canvassed subsequently in section 3.1, access to meson elastic form factors at EIC proceeds via a Sullivan process, which involves extrapolation to an off-mass-shell meson. The accuracy of this procedure is being quantified and validated by contemporary theory [44, 45].

Crucially, as explained in [13], section 4C], EIC is capable of providing precise pion form-factor data that will probe deep into the region where $F_\pi(Q^2)$ exhibits strong sensitivity to EHM and the evolution of this effect with scale. Furthermore, analyses presented, e.g. in [18], section 4B] and [38], section III], have stressed that if EIC can complement such pion information with precise $F_K(Q^2)$ data for a material domain above $Q^2 \approx 5\ \text{GeV}^2$, then it will be the first facility to deliver insights into the size and range of nonperturbative EHM–HB interference effects in hard exclusive processes.

#### 2.1.2. Pion and kaon distribution functions.

The pion valence quark distribution function (DF), $q^\pi(x,\zeta)$, expresses the probability density that a valence $q$-quark in the pion carries a light-front fraction $x$ of the system's total momentum at a resolving scale $\zeta$ [46]. Connected with this, and capitalising on the known behaviour of hadron wave functions at large valence-quark relative momenta [22, 47–49], numerous analyses within a diverse array of frameworks predict the following large-$x$ behaviour (see e.g. [50–54]):

$$q_\pi(x;\zeta=\zeta_H) \overset{x\simeq 1}{\approx} (1-x)^\beta, \quad \text{with } \beta = 2, \tag{6}$$

where $\zeta_H$ is the hadronic scale, which is not accessible in experiment because certain kinematic conditions must be met in order for the data to be interpreted in terms of $q_\pi(x,\zeta)$ [46]. Hence, any result for a DF at $\zeta_H$ must be evolved to $\zeta_E\ (>\zeta_H)$ for comparison with experiment [55–58]. Under such evolution, the exponent grows, viz $\beta = 2+\delta$, where $\delta$ is an anomalous dimension that increases logarithmically with $\zeta$. Significantly, within DF fitting uncertainties, the analogous behaviour for the proton's valence-quark DF has been confirmed [59].

It is worth noting here that what has come to be known as the Drell–Yan–West relation provides a link between the large-$x$ behaviour of DFs and the large-$Q^2$ dependence of hadron elastic form factors [60, 61]. In its original form, the relation was discussed for the $J=1/2$ proton. It has long been known that this original form is invalid when, e.g., the target is a ($J=0$) pseudoscalar meson and the valence-parton scatterers are $J=1/2$ objects [62, 63]. The generalisation to spin-$J$ targets composed of $J=1/2$ quarks may be found in [53]: for a hadron $H$ defined by $n+1$ valence $J=1/2$ partons, so that its leading elastic electromagnetic form-factor scales as $(1/Q^2)^n$:

$$q_H(x;\zeta_H) \overset{x\simeq 1}{\approx} (1-x)^p, \quad p = 2n-1+2\Delta S_z, \tag{7}$$

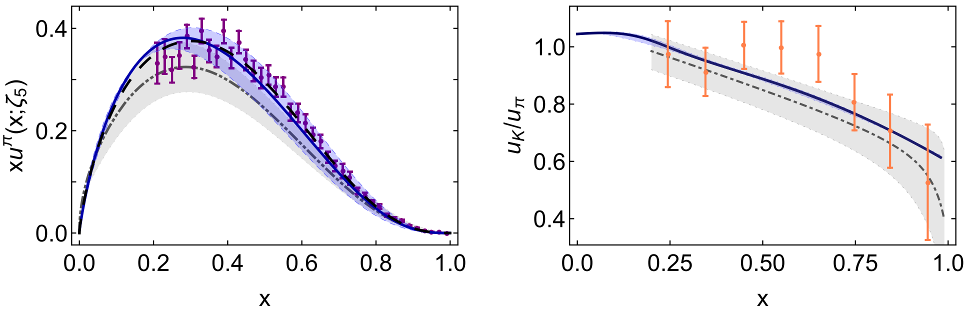

**Figure 3.** Left panel. Pion valence-quark momentum DF, $xq_\pi(x;\zeta_5 = 5.2\ \text{GeV})$: solid blue curve—modern continuum calculation [71, 72]; long-dashed black curve—early continuum analysis [75]; and dot-dot-dashed grey curve—lattice QCD result [73]. Data (purple) from [65], rescaled according to the analysis in [69]. Right panel. $u_K(x;\zeta_5)/u_\pi(x;\zeta_5)$. Solid blue curve—prediction from [71, 72]. Dot-dashed grey curve within grey band—lattice QCD result [76]. Data (orange) from [77]. Reproduced from [72]. CC BY 4.0.

where $\Delta S_z = |S_z^q - S_z^H|$. For a pseudoscalar meson, $n = 2$, $S_z^H = 0$, so $p = 2$. One thereby recovers equation (6).

Experiments interpretable in terms of $q_\pi(x,\zeta)$ were completed more than thirty years ago [64, 65]. Notably, phenomenological analyses of that data which ignore soft-gluon (threshold) resummation effects return a DF that roughly resembles a profile with $\beta \approx 1$ [66–68], in conflict with equation (6). On the other hand, [69], which included such next-to-leading-logarithm resummation using the 'cosine method', yields $\beta > 2$, in accord with equation (6). The dependence of the inferred large-$x$ behaviour of DFs on the resummation prescription is being explored [70]: preliminary findings suggest that, depending on the method adopted ('double Mellin', 'expansion' or 'cosine'), the apparent $\beta$ exponent can range between $\sim 1$ and $\sim 2.5$ at the input scale. Importantly, however, all methods yield softened large-$x$ behaviour, and both the *expansion* and cosine approaches produce $\beta > 2$. Additional remarks on these issues are presented in section 2.3.

The CSM prediction [71, 72] for $u_\pi(x;\zeta_5)$ is depicted in the left panel of figure 3. Its large-$x$ behaviour agrees with equation (6) and the pointwise form matches that determined in [69]. Regarding glue and sea DFs, [71, 72] provide parameter-free predictions for all pion DFs.

Notably, as described in section 2.2, lattice-regularised QCD is now beginning to yield results for the pointwise behaviour of the pion's valence-quark distribution [73, 74], and that delivered by the approach described in [73] is in fair agreement with both equation (6) and the CSM prediction. This is highlighted by the comparison between the blue CSM result and the dot-dot-dashed (grey) curve in the left panel of figure 3.

Parameter-free predictions for all kaon DFs are also provided in [71, 72]. Concerning valence-quarks, there are qualitative similarities between $u_K(x)$, $\bar{s}_K(x)$ and $u_\pi(x)$, e.g., all three DFs are consistent with equation (6), so that $\bar{s}_K(x)$ is much softer than the lattice-QCD result drawn in figure 5(left). There are also quantitative differences between the valence distributions, as highlighted by the prediction for $u_K(x)/u_\pi(x)$ drawn in figure 3(right) and compared with the result determined from a measurement of the $K^-/\pi^-$ structure function ratio [77].

The first lattice-QCD results for $u_K(x)/u_\pi(x)$ are also drawn in figure 3(right). The relative difference between the central lattice QCD result and the continuum prediction [71, 72] is $\approx 5\%$, despite the fact that the individual DFs from these two sources are qualitatively and quantitatively different. This feature highlights a long-known characteristic, i.e., $u_K(x)/u_\pi(x)$

is quite forgiving of even large differences between the individual DFs used to produce the ratio. Evidently, more precise data is crucial if this ratio is to be used effectively to inform and test the modern understanding of pion and kaon structures; and the results for $u_\pi(x;\zeta_5)$ and $u_K(x;\zeta_5)$ separately have greater discriminatory power. These remarks are amplified by the fact that the lone $K^-/\pi^-$ structure function experiment was performed forty years ago. Hence, new precision data and extractions must be a high priority.

Significantly, [71, 72] also provide the first parameter-free predictions for the ratios of glue and sea DFs in the pion and kaon. The kaon's glue and sea distributions are similar to those in the pion; but the inclusion of mass-dependent splitting functions, expressing Higgs-induced current-quark mass splittings, introduces differences in the valence-quark domain. Today, no empirical information is available that would enable these predictions to be tested. Hence, experiments sensitive to glue and sea distributions in the kaon and pion would be of enormous value.

Euclidean-space-based CSMs obtain the pion's DFs by considering it to be a bound state of a dressed-quark and a dressed-antiquark at the hadronic scale, where the sea and glue distributions are zero at $\zeta_H$ and generated by evolution on $\zeta > \zeta_H$ [78, 79]. This is also the case for the kaon. In contrast, a Minkowski space analysis of the Bethe–Salpeter equation finds that the valence-quark probability in the pion state is about 70% [80], with the remaining normalisation distributed among higher Fock-space components, carrying gluons at the hadronic scale. A resolution of this puzzle will likely be found in the mapping between the different quasi-particle degrees of freedom that serve in each calculation.

Related analyses of pseudoscalar meson generalised transverse-momentum-dependent DFs (GTMDs) are also becoming available [81]. They indicate that GTMD size and shape are also prescribed by the scale of EHM. Proceeding from GTMDs to generalised parton distributions (GPDs) [81–86], it is found that the pion's mass distribution form factor is harder than its electromagnetic form factor, which is harder than the gravitational pressure distribution form factor; the pressure in the neighbourhood of the pion's core is similar to that at the centre of a neutron star; the shear pressure is maximal when confinement forces become dominant within the pion; and the spatial distribution of transversely polarised quarks within the pion is asymmetric.

Regarding transverse momentum-dependent DFs (TMDs), these studies indicate that their magnitude and domain of support decrease with increasing twist [81]. Consistent with intuition [81], at $\zeta_H$, the simplest Wigner distribution associated with the pion's twist-two dressed-quark GTMD is sharply peaked in the kinematic domain associated with valence-quark dominance, has a domain of negative support, and broadens as the transverse position variable increases in size.

More sophisticated studies are beginning to appear. For instance, [86] computes and compares pion and kaon GPDs built using the overlap representation from light-front wave functions constrained by the one-dimensional valence distributions described above. It finds, *inter alia*, that $K$ pressure profiles are spatially more compact than $\pi$ profiles, and that near-core pressures in both NG modes are of a similar magnitude to that found in neutron stars. Plainly, now is the right time to plan to exploit the capacities of EIC to probe these higher-dimensional aspects of pion and kaon structure.

### *2.2. Pion and kaon structure—lattice QCD status*

Quantising QCD on a finite-volume discrete lattice in Euclidean space–time enables the numerical calculation of correlation functions defined by the functional integral [87]. Accessing hadron structural information using lattice QCD has been a very

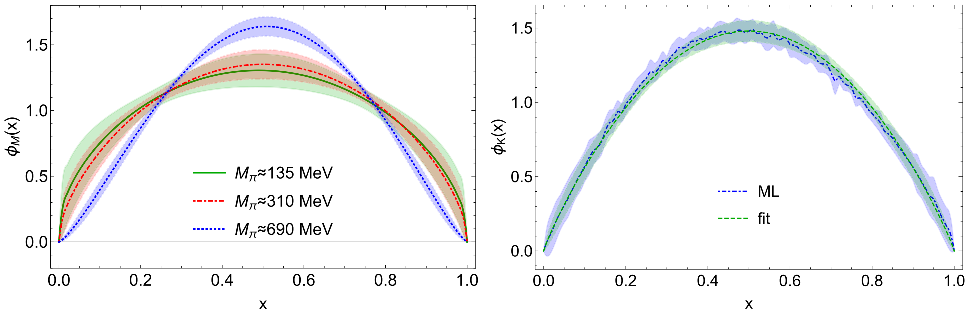

**Figure 4.** Left panel. $x$-dependent pion DA at two different pion masses, along with an extrapolation to the physical pion mass. As the pion mass decreases, the DA become broader. The calculations use a meson-boosted momentum of $P_z = 1.73$ GeV and are renormalised at 2 GeV in the $\overline{MS}$ scheme. Right panel. $x$-dependent kaon DA obtained using a fit to lattice results obtained through a machine-learning approach [103].

challenging task, since DFs are light-cone quantities and cannot be calculated directly on a Euclidean lattice. Over the years, a range of methods have been proposed to overcome this obstacle, such as studies based on the hadronic tensor [88–90], auxiliary quark-field approaches [91, 92], large-momentum effective theory (LaMET) [93–95] (Parton Distribution Functions (PDF)), pseudo-PDFs [96], an operator-product expansion-based method [97], and the good lattice cross-sections (LCS) approach [98–100]. These methods have some common ground, but also differences. Interested readers may consult [95, 101, 102] for more details. This subsection describes a few examples of recent progress in meson structural studies and indicates calculations that will be important for the success of EIC science.

*2.2.1. Meson distribution amplitudes.* The $x$-dependent quark DAs of the pseudoscalar mesons have been calculated both in the LaMET approach [74, 103] and using a current–current approach analogous to LCS [104, 105]. Reference [103] describes a study of the pion-mass dependence of the pion DA on the lattice in the continuum limit, as determined from three lattice spacings: 0.06, 0.09, 0.12 fm. Figure 4 shows pion DA results at pion masses of 690 MeV and 310 MeV, together with their extrapolation to 135 MeV. Note that the chiral extrapolation of [103] is dominated by the 310 MeV calculations. The lattice kaon DA is shown on the right-hand side of figure 4. The kaon DA is narrower than that of the pion, as suggested in [6, 106]. The variation of the DA shapes with quark mass helps in the understanding of the origin of mass [13].

*2.2.2. Meson parton distribution functions.* The advances in computing hadronic structure from calculations on a Euclidean lattice are transforming our ability to study the DFs of mesons within lattice QCD. Many of the challenges in capitalising on these advances mirror those encountered in the global fitting community, most notably in obtaining a faithful description of DFs from incomplete data; in the case of lattice calculations, the advent of exascale computing, the application of novel methods—such as Bayesian approaches, and machine learning offer the promise of enabling us to address and overcome these challenges.

*2.2.3. Valence quark distribution.* Valence quark distributions are the most widely studied distributions within lattice QCD and also the area where these new approaches have shown the most immediate impact. Notably, calculations of the $x$-dependent DFs of the pion have

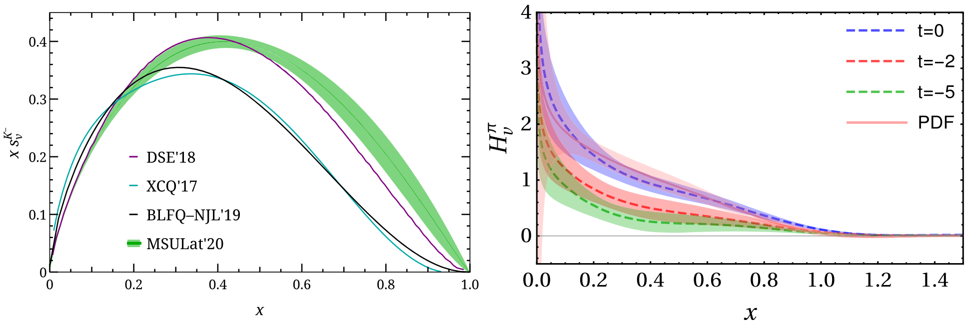

**Figure 5.** Left panel: lattice results for $x\bar{s}_v^K(x)$ as a function of $x$ (labelled as 'MSULat'20') [76]. Some model studies are shown for comparison. Additional discussion may be found elsewhere [[72], section 7.2]. Right panel: lattice results for the zero-skewness pion valence quark GPD $H_v^{\pi^+}(x, \xi = 0, t,\ \zeta = 4\ \text{GeV})$ for $t = \{0, -2, -5\}(2\pi/L)^2$ after one-loop matching and meson-mass corrections [110]. 'PDF' denotes the pion DF result in [74].

been performed for close-to-physical light-quark masses, with increasing control over the systematic uncertainties arising from the finite-volume and discretisation systematic uncertainties. Calculations have been performed within the LaMET [74, 76, 107], pseudo-PDF [108] and LCS frameworks [73, 109]. Most recently, these methods have been applied to the valence quark distributions of the kaon [76], as illustrated in figure 5, and the $u_K/u_\pi$ ratio, as discussed in connection with figure 3. These calculations are becoming comparable with extant data over a large range of $x$; and the arrival of the exascale era will enable them to be refined, especially with a view to the determination of the large-$x$ behaviour of the PDFs, whose significance is discussed in connection with equation (6).

*2.2.4. Gluon distribution.* Within lattice QCD, gluonic and flavour-singlet quantities are much noisier than valence-quark distributions. Thus, a far larger statistical sample is required to reveal a signal. The first exploratory gluon DF study applied the quasi-PDF approach to the gluon DFs [111], using ensembles with unphysically heavy quark masses corresponding to pion masses of 340 and 678 MeV. Unfortunately, the noise-to-signal ratio grows rapidly with the dimensionless parameter $zP_z$ and only the coordinate-space gluon quasi-PDF matrix element ratio results are presented. Since then, there have also been developments in improving the operators for the gluon DF lattice calculations [112–114], which should enable evaluation of the continuum limit in future lattice calculations of gluon DFs. The pseudo-PDF approach developed in [112], along with improved methods of calculation for reaching a higher boosted momentum, have recently been used to provide the first result for the nucleon gluon DF [115]. The prospects for applications to the cases of the pion and kaon appear promising, so that one may anticipate the appearance of increasingly precise calculations over the next few years.

*2.2.5. Pion GPDs.* In [110], the pion valence quark GPD at zero skewness was calculated using clover valence fermions on an ensemble of gauge configurations with $2 + 1 + 1$ flavours (degenerate up/down, strange and charm) of highly-improved staggered quarks with a lattice spacing of $a \approx 0.12$ fm, a box size of $L \approx 3$ fm and a pion mass of $m_\pi \approx 310$ MeV. The result is shown in figure 5—right. It turns out that, with current uncertainties, the result does not show a clear preference among different model assumptions about the kinematic dependence of the GPD. To distinguish between different models, further studies with better statistics will be crucial.

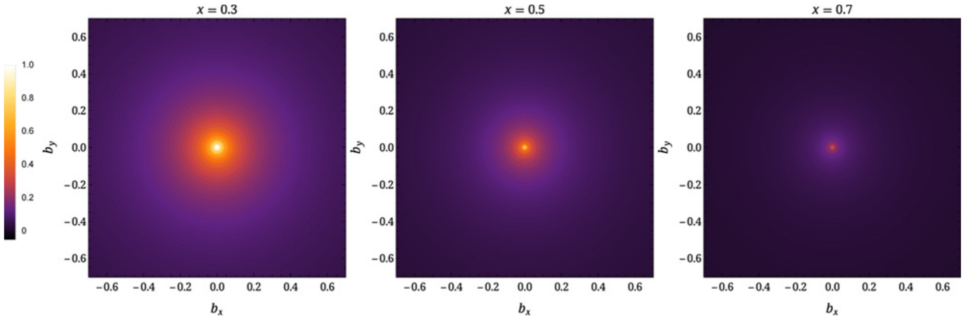

**Figure 6.** The two-dimensional impact-parameter-dependent distribution, $\mathsf{q}(x, b)$, for $x = 0.3$, 0.5, and 0.7 determined from a lattice-QCD calculated pion GPD at physical pion mass.

One may therefore anticipate that there will be lattice calculations of the pion's valence quark GPD, $H_\pi(x, \xi = 0, Q^2)$, within the next few years. The Fourier transform of this GPD gives the impact-parameter-dependent distribution, $\mathsf{q}(x, b)$ [116, 117]:

$$\mathsf{q}(x, b) = \int \frac{\mathrm{d}\mathbf{q}}{(2\pi)^2} H_\pi(x, \xi = 0, t = -\mathbf{q}^2)\mathrm{e}^{\mathrm{i}\mathbf{q}\cdot\mathbf{b}}, \tag{8}$$

where $b$ is the light-front distance from the transverse centre of momentum (CoTM). Figure 6 shows the two-dimensional distributions at $x = 0.3, 0.5,$ and $0.7$. The impact-parameter-dependent distribution describes the probability density for a parton with a momentum fraction $x$ to be found in the transverse plane at a distance $b$ from the CoTM. It provides a snapshot of the pion in the transverse plane and indicates what might be expected from nucleon tomography.

### 2.3. Global QCD analysis

Extracting information about DFs (or any partonic content of hadrons) from experimental data is a challenging problem in hadronic physics. Since the Lagrangian partons can never be isolated as free particles, details about their properties must be inferred indirectly by exploiting theoretical tools, such as QCD factorisation theorems [118]. The latter allow experimental observables in certain kinematic regions, viz $M_N^2/[(1-x)Q^2] \ll 1$, to be written as convolutions of perturbatively-calculable hard-scattering cross-sections and nonperturbative DFs parametrising long-distance quark-gluon physics. The most robust method for extracting information about DFs from experiment is through global QCD analyses of various QCD-factorisable hadronic processes that are sensitive to different combinations of DFs [66, 67, 70, 119–124].

Historically, the main experimental observables that have been used to constrain pion DFs have come from pion–nucleus collisions with the inclusive production of lepton pairs or prompt photons [64, 65, 125]. More recently, leading neutron electroproduction data [126, 127] have been used to constrain pion DFs at small $x$, assuming the validity of pion exchange at small values of the transverse momentum and large values of the longitudinal momentum of the produced neutron [126–128].

Important questions remain, however, concerning the fraction of the pion's momentum carried by gluons relative to the valence and sea quarks, and the behaviour of DFs at small and large values of $x$. For the latter, many calculations have been completed, and the exponent on $(1-x)^\beta$ ranges from $\beta \sim 0$ to $\beta \sim 2$. This was highlighted in [129] and in a raft of calculations since then, e.g. [71, 72, 78, 79, 81, 130–136]. In model calculations [81, 130–136],

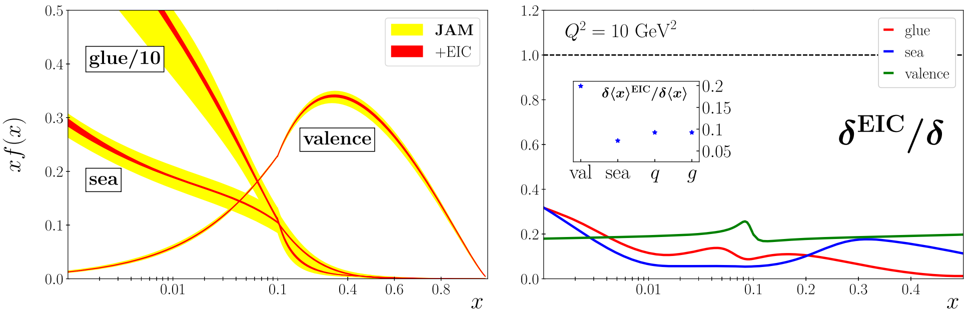

**Figure 7.** Left panel. Comparison of uncertainties for the pion's valence, sea quark, and gluon PDFs before (yellow bands) and after (red bands) the inclusion of EIC data. Right panel. Ratio of uncertainties between the 'with EIC data' and 'without', $\delta^{\mathrm{EIC}}/\delta$, valuesversions of the valence (green line), sea quark (blue) and gluon (red) PDFs, assuming a 1.2% experimental systematic uncertainty but no model systematic uncertainty, and (inset) the corresponding ratios of the momentum fraction uncertainties, $\delta\langle x\rangle^{\mathrm{EIC}}/\delta\langle x\rangle$, for the valence, sea, total quark, and gluon PDFs [70], at a scale $Q^2 = 10\ \mathrm{GeV}^2$.

the energy scale and the value of $x$ at which the asymptotic behaviour should be evident are *a priori* unknown. On the other hand, as noted in connection with equation (6), all calculations that enable a connection to be drawn between the underlying meson-binding dynamics and the valence-quark DF show that $\beta$ is determined by the behaviour of the quark–antiquark interaction. Concerning data analyses, as already noted, inclusion and/or the treatment of soft-gluon resummation can affect the inferred large-$x$ PDF behaviour [69, 70, 137–140], and the interplay of resummation and fixed-order calculations needs to be better understood.

The detailed $x$ dependence of pion DFs is clearly a topic of considerable theoretical and phenomenological interest, and more data over a large range of kinematics would be helpful to unravel this structure. A leading programme of baryon production in inclusive deep inelastic scattering (DIS) from the deuteron with proton tagging ('TDIS') at Jefferson Lab [141] aims to explore the structure of pions emitted from the bound neutron [142], with generalisation to the hyperon case [143] aimed at investigating corresponding kaon structural observables. Complementing Hadron-Electron Ring Accelerator (HERA) and JLab measurements, EIC data on leading neutron and hyperon production can provide information about the role of the nucleon's peripheral structure in a unique region by interpolation between these kinematics. Especially in this interpolation region, EIC's combination of high precision and wide kinematical coverage from $Q^2 \sim$ [few $\mathrm{GeV}^2$] to $Q^2 \sim O(100\ \mathrm{GeV}^2)$ suggests a significant potential to constrain scaling violations in the pion structure function. This, in turn, may afford a higher level of discriminatory power to unravelling the pion's gluon content from the corresponding valence-/sea-quark contributions.

The potential impact of EIC neutron production data is illustrated in figure 7, which shows the valence, sea quark, and gluon PDFs in the pion from the Jefferson Lab Angular Momentum Collaboration (JAM) global QCD analysis at the evolved scale $Q^2 = 10\ \mathrm{GeV}^2$ [66], comparing current uncertainties with those expected following the addition of EIC data [70]. The analysis of the existing data includes pion–nucleus Drell–Yan cross-sections, both $p_{\mathrm{T}}$-differential and $p_{\mathrm{T}}$-integrated, and the leading neutron structure functions from HERA [144]. The analysis assumes a centre-of-mass (CM) energy $\sqrt{s} = 73.5$ GeV for an integrated luminosity $\mathcal{L} = 100\ \mathrm{fb}^{-1}$ and a 1.2% systematic uncertainty across all kinematics. For both the sea quark and gluon distributions, the PDF uncertainties are reduced by a factor $\sim 5$–10 for most of the $x$ range, with a similar factor of $\sim 5$ reduction in the valence sector. For

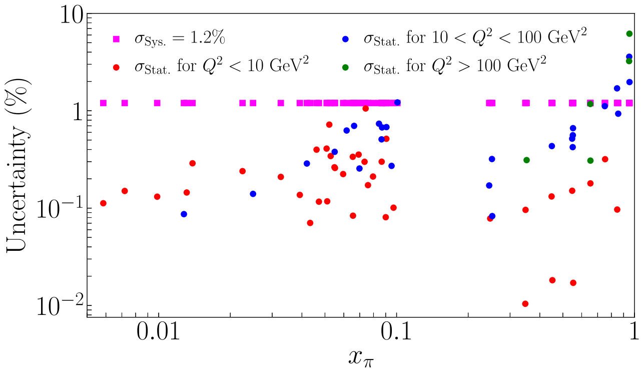

**Figure 8.** Fractional uncertainties of the cross-sectional projected data as used for the pion PDF impact analysis in figure 7. The statistical uncertainties $\sigma_{\text{Stat.}}$ are shown as circles, separated in colour by the ranges in $Q^2$. The assumed systematic uncertainties $\sigma_{\text{Sys.}}$ of 1.2% are shown by magenta squares.

a decomposition of the pion mass written in terms of QCD stress–energy tensor matrix elements [145], the first moments, $\langle x \rangle_{q,g}$, are relevant. However, as discussed in connection with figure 1, the meaning of such a frame- and scale-dependent decomposition is uncertain [[4], section V], [[5], sections 4.4 and 4.5]. Notwithstanding that, such moments are interesting in themselves, so it is worth noting that the reduction in associated uncertainties is a factor of $\approx 10$ for both the total quark and gluon contributions, as can be seen in the inset of figure 7(right). Note, however, that the errors do not include uncertainties associated with the model dependence of the 'pion flux,' which may be of the order of 10%–20% [126, 127], and might reduce the impact of the projected data on the pion PDF uncertainties. A similar analysis may be performed for the PDFs in the kaon, which can be obtained from leading hyperon production in the forward region. In this case, the near-absence of empirical information on the parton structure of kaons means that new EIC data will have an even more striking impact.

For the impact study of the pion PDFs, the uncertainties of the differential cross-section were used. These are shown in figure 8 as a function of $x_\pi$ and further discussed in section 5.1. The systematic uncertainty is 1.2% (magenta squares); the statistical uncertainties are, on average, less than 0.5%, and vary as a function of $x_\pi$ and $Q^2$ (filled circles). The statistical uncertainty is smallest at small values of $x_\pi$ and $Q^2$, and increases with increasing values of $x_\pi$ and $Q^2$. Clearly, for much of the range $x_\pi \lesssim 0.8$, the systematic uncertainties dominate the statistical uncertainties. This was not the case with the same observable in the HERA experiments [126, 127]. Because the integrated luminosity for the EIC is projected to be about three orders of magnitude greater than that of HERA, the total uncertainty quantification will be largely driven by the systematic uncertainties.

### 2.4. Synergy between theory calculations and data analysis

In comparison with the nucleon, experimental probes of the pion and kaon have been relatively sparse, and substantial ambiguities remain regarding their partonic, quark-gluon substructure. Partly for this reason, one may expect future knowledge of the pion to be derived from an interplay between several methods (see figure 9): QCD phenomenology, including QCD-inspired models and continuum methods in Euclidean and Minkowski spaces; recent developments in lattice QCD; and QCD global analyses of both contemporary and future data. For the latter,

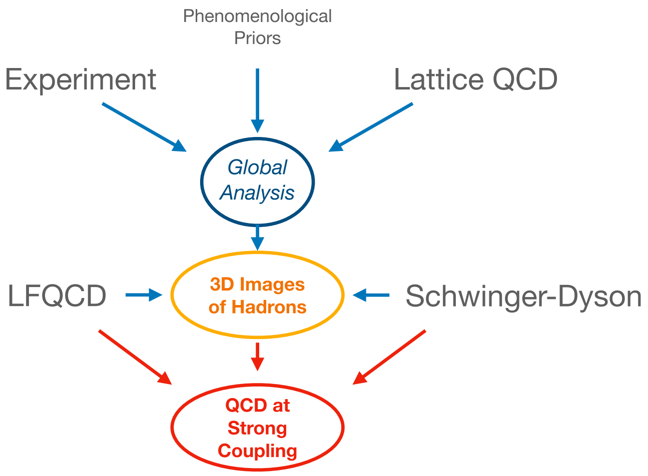

**Figure 9.** Potential interplay between QCD phenomenology, continuum approaches to QCD, lattice, global analysis and experiment.

EIC can be expected to furnish a significant amount of valuable data; and therefore to be a crucial driver of global theoretical efforts. Naturally, in the context of this discussion, the focus here is on the structure of NG modes as quantified via collinear parton distribution functions (PDFs), or, in the case of three-dimensional structures, GPDs and TMDs.

To explore possible synergies among the approaches sketched above, a number of theoretical issues require further development and understanding. The following are especially prominent.

- **Direct lattice calculation of distributions**. A major advance in the ability to study the internal structure of hadrons from lattice QCD computations was the realisation that PDFs, and their three-dimensional extensions, described as matrix elements of operators separated along the light cone, could be related to quantities calculable in Euclidean space [93, 94, 100, 146]. Such calculations do not yield a pointwise evaluation of the PDFs at each Bjorken-$x$, but rather convolutions of those PDFs with some calculable kernel, together with modifications in the manner of higher-twist and mass corrections. The resulting convolutions in practical lattice calculations yield functions that are incomplete and limited by the finite volume and discretisation of the lattice. The extraction of the $x$-dependent PDFs from such calculations therefore requires that an inverse problem be addressed, whose solution requires additional information.

This situation somewhat mirrors that of global fits to experimental data, in which the desired PDFs generally arise, as in Drell–Yan processes, from a convolution with a perturbatively calculated kernel. For the case of one-dimensional distributions, such as PDFs, the additional information can be provided through an assumed PDF parametrisation, so that extraction of the PDF becomes a parameter-fitting exercise. That method has been central to the strategy of the global fitting community and has likewise been adopted by several lattice collaborations. More recently, there has been an effort to incorporate different schemes, such as machine learning and Bayesian reconstruction [147, 148].

- **Inclusion of lattice results as data in QCD global analyses**. An evolving opportunity is to introduce results from lattice computations into the global fits [149], either in the same manner as experimental data, in the case of the nucleon PDFs [150], or as a Bayesian prior in the fit to experimental data, as was accomplished for the nucleon tensor charge [151]. The aim, at least for the nucleon, is not to test QCD, but rather to use both experiment and lattice computations to provide more information about key measures of hadron structure than are possible using either computation alone. For pions and kaons, for which there are no free meson targets and the structure is indirectly probed using the Sullivan process at the EIC, lattice computations of the PDFs of a lone, isolated pion or kaon may assist in validating the experimental analysis, potentially providing benchmarks to quantify the effects of off-shellness or kinematical extrapolations in $t$;

Lattice computation and experiment may also provide complementary information on hadron structure. Thus, the computation of gluon and flavour-singlet contributions to hadron structure is an important effort, and those computations may predict the outcomes of experiment. Similarly, recent developments have enabled the calculation of the $x$-dependent GPDs, both for the nucleon [152, 153] and the pion [110]—see figure 5(right), and the frameworks allow these distributions to be extracted at definite non-zero skewness [152, 154].

- **Benchmarking calculations with QCD fits and phenomenology**. PDF (or GPD/TMD) phenomenology can offer benchmarks for use in developing lattice and/or continuum QCD computations; in particular, the Next-to-Next-to Leading Order (NNLO) precision of contemporary *nucleon* PDF analyses in the unpolarised sector is such that these extractions can play an important role in testing analogous calculations of lattice quantities, such as PDF Mellin moments [155]. Similar arguments apply to the recent QCD global analyses of meson structure noted above.
- **Relating Euclidean lattice QCD and continuum methods**. A number of formal developments related to treatments of the pion using CSMs, including Dyson–Schwinger equations and light-front quantisation would also be helpful. Lattice studies long ago confirmed the continuum predictions of nonperturbative infrared dressing of gluons and quarks, which are the effective degrees of freedom in the pion/kaon exploited by continuum methods. The light-front projection of a hadron's Bethe–Salpeter amplitude [28, 34] is linked to a Fock component in a basis whose character is specified by the resolving scale [72, section 2]. This projection is a gauge-invariant probability density [156]. The hadron image on the null-plane [157], expressed by Ioffe time and the transverse coordinates of dressed constituents, may be accessible along this path [158, 159];
- **Mapping the pion light-front wave function**. Understanding QCD on the null plane will place the concept of the light-front wave function on firmer ground, allowing access to pion PDFs, GPDs, TMDs, and more [14] within a unified, invariant representation of the meson. A clear identification of the unitary transformation from the free light-front Fock-space basis to the one that entails dressed and confined constituents is necessary. To this end, investigations into the non-triviality of the vacuum and the role of zero-modes in light-front quantisation are ongoing (see, e.g., [160–164]).

It is worth reiterating that data supplied by EIC will provide a firm basis for new insights into pion and kaon structure. By significantly expanding the world's pool of data that are sensitive to light-meson structural functions, EIC will provide a setting to explore and refine the synergies enumerated above and sketched in figure 9. These refinements will occur along several tracks, providing new constraints to QCD fits of meson parton distributions, which will then be used to inform and validate continuum analyses in QCD and phenomenological calculations, while also benchmarking rapidly-developing lattice efforts. These, in turn, can be expected to serve reciprocally as guidance for, and constraints on, QCD fits of data, including the highly anticipated EIC measurements envisioned in this work.

**Table 1.** Scientific questions related to pion and kaon structure and our understanding of the emergent-hadron mass mechanism possibly accessible at an EIC, with the key measurements and some key requirements. Further requirements are addressed in the text.

| Scientific question | Key measurement [1] | Key requirements [2] |
|---|---|---|
| What are the quark and gluon energy contributions to the pion mass? | Pion structural function data over a range of $x$ and $Q^2$ | • Need to uniquely determine $e + p \to e' + X + n$ (low $-t$)<br>• CM energy range $\sim$ 10–100 GeV<br>• Charged-neutral currents desirable |
| Is the pion full or empty of gluons as viewed at large $Q^2$? | Pion structural function data at large $Q^2$ | • CM energy $\sim$ 100 GeV<br>• Inclusive and open-charm detection |
| What are the quark and gluon energy contributions to the kaon mass? | Kaon structural function data over a range of $x$ and $Q^2$ | • Need to uniquely determine $\Lambda,\Sigma^0$: $e + p \to e' + X + \Lambda/\Sigma^0$ (low $-t$)<br>• CM energy range $\sim$ 10–100 GeV |
| Are there more or less gluons in kaons than in pions as viewed at large $Q^2$? | Kaon structural function data at large $Q^2$ | • CM energy $\sim$ 100 GeV<br>• Inclusive and open-charm detection |
| Can we get quantitative guidance on the emergent pion mass mechanism? | Pion form-factor data for $Q^2 = 10\text{–}40$ (GeV/c)$^2$ | • Need to uniquely determine exclusive process $e + p \to e' + \pi^+ + n$ (low $-t$)<br>• $e$–$p$ and $e$–$d$ at similar energies<br>• CM energy $\sim$ 10–75 GeV |
| What is the size and range of interference between emergent mass and the Higgs-mass mechanism? | Kaon form-factor data for $Q^2 = 10\text{–}20$ (GeV/c)$^2$ | • Need to uniquely determine exclusive process $e + p \to e' + K^+ + \Lambda$ (low $-t$)<br>• L/T separation at CM energy $\sim$ 10–20 GeV<br>• $e$–$p\Lambda/\Sigma^0$ ratios at CM energy $\sim$ 10–50 GeV |
| What is the difference between the impacts of emergent- and -mass mechanisms on light behaviour? | Behaviour of (valence) up quarks in pions and kaons at large $x$ | • CM energy $\sim$20 GeV (lowest CM energy to access large -$x$ region)<br>• Higher CM energy for range in $Q^2$ desirable |
| What is relationship between dynamic chiral symmetry breaking and confinement? | Transverse-momentum-dependent fragmentation of the functions of quarks into pions and kaons | • Collider kinematics desirable (compared to fixed-target kinematics)<br>• CM energy range $\sim$ 20–140 GeV |
| **More speculative observables** | | |
| What is the trace anomaly contribution to the pion mass? | Elastic $J/\psi$ production at low $W$ off the pion | • Need to uniquely determine $e + p \to e' + \pi^+ + J/\Psi + n$ (low $-t$)<br>• High luminosity ($10^{34+}$)<br>• CM energy $\sim$ 70 GeV |
| Can we obtain tomographic of the pion in transverse plane?<br>What is the pressure distribution in a pion? | Measurement of Deeply Virtual Compton Scattering (DVCS) from a pion target as defined using the Sullivan process | • Need to uniquely determine $e + p \to e' + \pi^+ + \gamma + n$ (low $-t$)<br>• High luminosity ($10^{34+}$)<br>• CM energy $\sim$ 10–100 GeV |
| Are transverse momentum distributions universalpions and protons? | Hadron multiplicities Semi-Inclusive Deep Inelastic Scattering (SIDIS) from a pion target as defined using the Sullivan process | • Need to uniquely determine scattered off pion: $e + p \to e + h + X + n$ (low $-t$)<br>• High luminosity ($10^{34+}$)<br>• $e$–$p$ and $e$–$d$ similar energy desirable<br>• CM energy $\sim$ 10–100 GeV |

## 3. Key EIC measurements

It is necessary here to summarise the experimental requirements for critical EIC measurements that tackle some outstanding questions in the study of pion and kaon mass and structure. This will subsequently lead to an explanation of how these meson structural measurements, which serve as a laboratory in which the fundamental aspects of QCD can be elucidated, complement and strengthen ongoing and expected programmes worldwide.

To facilitate this discussion, it is useful to translate the current theoretical understanding of light meson structure and emergent hadron mass (and structural) mechanisms into a set of critical science questions. Currently, not all these science questions are rigorously defined theoretically; but they do reflect the current state of understanding. These questions come from community discussions at a series of dedicated pion/kaon structural workshops (2017, 2018, 2019, and 2020), and at meetings related to the EIC Yellow Report activities in 2020. Indeed, the EIC Yellow Report [165] includes an overview of meson structural measurements and their requirements for EIC detector design based on the detailed work presented here. The scientific questions represent outstanding mysteries that require further experimental (and theoretical) examination, and illustrate the impact of a coherent study of pion and kaon structure that would yield results similar to present studies of proton structure.

Table 1 lists the key science questions along with specific measurements required to advance community understanding. It also presents the high-level experimental needs, providing the minimum experimental requirements as well as improvements that could further expand these studies. Later sections will examine other important considerations that aim to demonstrate that one can extract pion and kaon structural information independently of the phenomenology ansatz, independently of physics background contributions, and independently of Mandelstam-$t$. Some interesting science questions that may be more challenging to address are listed at the bottom of the table; they are considered more speculative, because validating the reaction mechanism will be more challenging than the other cases, owing to considerations such as competing reaction and background mechanisms.

For all observables, a luminosity well above $10^{33}$ is required to compensate for the (few times) $10^{-3}$ fraction of the proton wave function related to the pion (kaon) Sullivan process. Also, a large range in $x_{\mathrm{L}}$ (the longitudinal energy fraction carried by the produced particle) is required, up to $x_{\mathrm{L}} \sim 1$ for ep reactions and an $x_{\mathrm{L}}$ of at least $\sim 0.5$ for ed reactions. Data about negatively-charged pions (e.g. $e + d \rightarrow e^{'} + p + p + X$) and about neutral-pion channels (e.g. $e + p \rightarrow e' + p + X$) are crucial to constrain reaction mechanisms and theoretical backgrounds when extracting the physical pion (kaon) target information.

### 3.1. Sullivan process

In specific kinematic regions, the observation of recoil nucleons (N) or hyperons (Y) in the semi-inclusive reaction $ep \rightarrow e'(\mathrm{N\,or\,Y})X$ can reveal features associated with correlated quark–antiquark pairs in the nucleon, referred to as the 'meson cloud' of the nucleon. At low values of $|t|$, the four-momentum transfer from the initial proton to the final nucleon or hyperon, the cross-section displays a behaviour characteristic of meson pole dominance. The reaction in which the electron scatters off the meson cloud of a nucleon target is called the Sullivan process [166]. For elastic scattering ($X = \pi^+$ or $K^+$), this process carries information about the pion's or kaon's form factor, and could be tagged by the detection of a recoil nucleon or hyperon, respectively. For DIS, the typical interpretation is that the nucleon parton distributions contain a mesonic parton content. To access pion or kaon partonic content via such a structural function measurement requires scattering from a meson target, which again could be facilitated in the Sullivan process by the detection of a recoil nucleon or hyperon.

The Sullivan process can provide reliable access to a meson target in the space-like $t$ region, if the pole associated with the ground-state meson remains the dominant feature of the process and the structure of the related correlation evolves slowly and smoothly with virtuality. To check whether these conditions are satisfied empirically, one can take data covering a range of $t$, particularly low $|t|$, and compare them with phenomenological and theoretical expectations. A recent calculation [44] explored the circumstances under which these conditions should be satisfied. For the pion (kaon) Sullivan process, a low $-t$ equates to $-t < 0.6$ (0.9) $\mathrm{GeV}^2$ to be able to cleanly extract the pion (kaon) structure, and data over a range of $-t$ down to the lowest accessible value are needed to verify pion (kaon) structural extraction.

### *3.2. Theoretical backgrounds in extracting the data*

The extraction of the mesonic structure of the nucleon from the tagged DIS cross-section is inherently model dependent. It will, therefore, be necessary to examine all the reasonable models that are available (such as Regge models of baryon production and models inspired by the Dyson–Schwinger equation), or that may be available in the future, to evaluate the theoretical uncertainty associated with extracting meson structural functions from the tagged deep inelastic data. To clarify this model dependence, one can formally write, e.g., the measured semi-inclusive structural function of the leading proton, $F_2^{\mathrm{LP}(4)}$, related to the measured cross-section as:

$$\frac{\mathrm{d}^4\sigma(ep \to e'Xp')}{\mathrm{d}x\,\mathrm{d}Q^2\,\mathrm{d}y\,\mathrm{d}t} = \frac{4\pi\alpha^2}{xQ^4}\left[1 - y + \frac{y^2}{2\,(1+R)}\right] F_2^{\mathrm{LP}(4)}(x, Q^2, y, t), \tag{9}$$

$y = P \cdot q/P \cdot l$, where $P(P')$ are the initial (scattered) proton four-vectors, $l(l')$ are the initial (scattered) lepton vectors, and $R$ is the ratio of the cross-sections of longitudinally and transversely polarised virtual photons. The measured cross-section can be integrated over the proton momentum (which is effectively an integration over $t$ [167]) to obtain the leading proton structural function $F_2^{\mathrm{LP}(3)}$. The pion structural function $F_2^{\pi}$ can then be extracted from $F_2^{\mathrm{LP}(3)}$ *using models*, such as the Regge model of baryon production. In the Regge model, the contribution of a specific exchange $i$ is defined by the product of its flux $f_i(y, t)$ and its structural function $F_2^i$ evaluated at $(x_i, Q^2)$. Thus,

$$F_2^{\mathrm{LP}(3)} = \sum_i \left[\int_{t_0}^{t_{\min}} f_i(z, t)\mathrm{d}t\right] F_2^i(x_i, Q^2), \tag{10}$$

where $i$ is the pion, $\rho$-meson etc, and $t$ corresponds to the range of $p_{\mathrm{T}}$ analysed.

Neglecting uncertainties in the evaluation of $R = \sigma_{\mathrm{L}}/\sigma_{\mathrm{T}}$, which should be a small quantity, the extraction of the pion structural function will have to be corrected for a number of complications to the simple Sullivan picture. These include non-pion pole contributions, $\Delta$ and other $N^*$ resonances, absorptive effects, and uncertainties in the pion flux. For example, the cross-section of leading charged pion production from the neutron is reduced by about twice by absorptive corrections from other mesons. While these corrections can be large, and one cannot extract the pion structural function without their inclusion, detailed calculations do exist [168]. Moreover, these corrections can be minimised by measuring at the lowest $-t$ or tagged nucleon momentum possible from the reaction. This minimises the absorptive correction since, at lower momenta, the pion cloud is further from the bare nucleon. In addition, the low momentum ensures that the higher meson mass exchanges are suppressed by the energy denominator. Also, the charged pion exchange process has the advantage of less background due to Pomeron and Reggeon processes [169], and the charged pion cloud is expected to be roughly double the size of the neutral pion cloud in the proton.

Obtaining data from *both* protons and deuterons will allow essential cross-checks of the models used in the extraction of the pion structural function. In the Regge model, it is assumed that the neutral pion, the Pomeron and the $f_2$ will be the leading contributions to the cross-section from the proton, while the charged pion, $\rho$ and $a_2$ are the leading contributions from the neutron [170, 171]. However, Regge phenomenology also predicts that the flux of Reggeons with isospin one ($\rho$ and $a_2$) account for only $\approx 3\%$ of the flux of Reggeons with isospin zero ($\omega$ and $f_2$) [170]. It also predicts that, for the neutron, the contributions from charged pion exchange are an order of magnitude larger than the contributions from $\rho$ and $a_2$ [168]. Pomeron exchange does not make a significant contribution, since diffractive dissociation is believed to be $\approx 6\%$ of the pion exchange contribution [168].

The measured tagged cross-sections and the extracted tagged structural functions can be analysed within a Regge framework where, assuming the dominance of a single Regge exchange, the differential cross-section for recoil baryon production as a function of $z$ at fixed $t$ should be proportional to $z - n$, where $n = 2\alpha(t) - 1$, and $\alpha(t)$ specifies the Regge trajectory of the dominant exchange. For pion exchange, the $n$ averaged over the $t$ dependence is expected to be $n \approx -1$, while other Reggeons are expected to have $n > -1$. Thus, by comparing the $z$ dependence of the cross-sections of proton and neutron (deuteron) scattering, it should be possible to determine the dominant exchange mechanism(s). Further, if the predictions for pion exchange are found to describe the data, the pion flux from the Regge model fits to hadron–hadron data may be safely used to extract the pion structural function.

The largest uncertainty in extracting the pion structural function, however, is likely to arise from the (lack of) knowledge of the pion flux in the framework of the pion cloud model. One of the main issues is whether to use the $\pi NN$ form factor or the Reggeised form factor. The difference between these two methods can be as much as $20\%$ [172]. From the $N - N$ data, the $\pi NN$ coupling constant is known to $5\%$ [173]. If we assume that all corrections can be performed with a 50% uncertainty, and we assume a 20% uncertainty in the pion flux factor, the overall theoretical, systematic uncertainty could approach $25\%$. The superior approach is to make a direct measurement of the pion flux factor by comparing it with pionic Drell–Yan data. For example, the pion structural function at $x = 0.5$ has been measured using pionic Drell–Yan data to an accuracy of $5\%$ (see, e.g. [65, 174]). New data from Common Muon and Proton Apparatus for Structure and Spectroscopy (COMPASS) should enable this possibility to be leveraged further and is likely to reduce the projected uncertainties even more.

### *3.3. Kinematics of interest that address specific theoretical questions*

The scientific questions of interest summarised in table 1 require a range of physics processes, spanning from (tagged) inclusive structural function measurements to (tagged) exclusive measurements, such as those required for a form-factor determination or meson femtography. In general, a large range of CM energies is required to access a wide range of $x$ and $Q^2$, as is relevant for pion (kaon) structural function measurements or hadron multiplicity measurements for a TMD programme. This has to be balanced against the requirement to uniquely determine the remnant nucleon (or $\Lambda$ or $\Sigma^0$) to ensure that the scattering process occured off a pion (kaon). The latter favours moderate CM energies, so as to be able to uniquely determine the remnant $\Lambda$ (or $\Sigma^0$), both for missing-mass determination and to ensure their decays occur before detection. In addition, there is a need for both ep and ed measurements at similar CM energies to validate the reaction mechanism and understanding. This drives the ‘typical’ CM energy range for pion and kaon structural function measurements to $\sim$ 10–100 GeV. Higher CM energies would increase the range of $Q^2$. On the other hand, lower CM energies are preferable for accessing the large-$x$ region to determine the behaviour of the valence quarks in pions (or kaons). In this

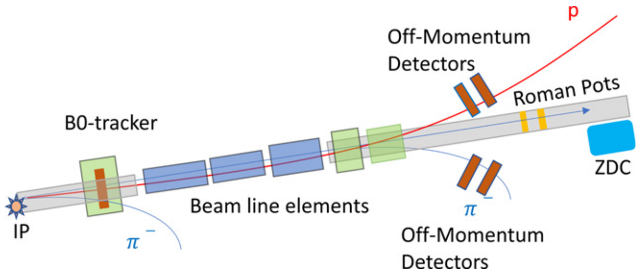

**Figure 10.** A sketch of the integrated beamline and detector setup in the far-forward area, along the direction of the proton/ion beam. The sketch is not to scale. The initial B0-tracker is integrated into the warm area of a combined electron–proton/ion beam magnet. A set of beamline magnetic elements then follows, which is integrated in one cryostat. This is followed by off-momentum detectors that capture the charged-particle decay products, Roman pots that capture far-forward-going protons with nearly the energy of the proton/ion beams, and the ZDC to capture far-forward-going neutral particles.

case, the figure of merit, folding in all kinematic effects, is optimised at the lowest CM energy that provides a sufficiently large $Q^2$ for a clean interpretation of the data.

For pion (kaon) fragmentation processes, the collider kinematics greatly facilitate transverse-momentum-dependent measurements at low scales ($p_T < 1$ GeV), and the largest range of CM energy is required. For some processes, the exact CM energy is not that important, so long as one obtains sufficient phase space for particle electroproduction to boost the experimental cross-section. For instance, this is true for the (deep) exclusive $J/\Psi$ measurements that possibly constrain the QCD trace anomaly, and also for access to charged-current cross-sections.

For pion (kaon) form-factor determination, the situation is different. The standard method relies on Rosenbluth L/T-separated cross-sections, as the longitudinal (L) cross-section enhances pion (kaon) pole sensitivity. Such measurements are best done at a relatively low CM energy range ($\sim$ 10–20 GeV). An alternate method to extract the pion form factor makes use of a direct comparison of charged-pion cross-sections for ep and ed. This method may be applicable up to higher CM energies (and higher $Q^2$ values). Similarly, for the kaon form factor, it may be possible to increase the $Q^2$ range (as compared to that from L/T-separated cross-sections) using the $\Lambda/\Sigma^0$ cross-section ratios. The latter requires further study, but is only possible at CM energies of $\sim$10–50 GeV, where the $\Lambda$ and $\Sigma^0$ may be cleanly isolated.

### *3.4. Complementarity with other facilities*

The broad science programme required to understand pion and kaon structures and the QCD mechanism behind the emergent hadron masses requires a strong interplay between experiment and theory, matching experimental prospects with new theoretical insights, rapid computational advances, and high-level QCD phenomenology. The EIC will play a key role in the experimental programme to chart in-pion and in-kaon distributions of, *interalia*, mass, charge, magnetisation, and angular momentum. Nonetheless, to provide experimental measurements that guide theoretical understanding requires a coherent, worldwide effort.

The unique role of the EIC is its access to pion and kaon structures over a wide range of large CM energies: $\sim$ 20–140 GeV. The Jefferson Lab will provide, at its CM energy of $\sim$ 5 GeV, tantalising data for the pion (kaon) form factor up to $Q^2 \sim 10(5)$ GeV$^2$, and measurements of the pion (kaon) structural functions at large-$x$ ($> 0.5$) through the Sullivan process.

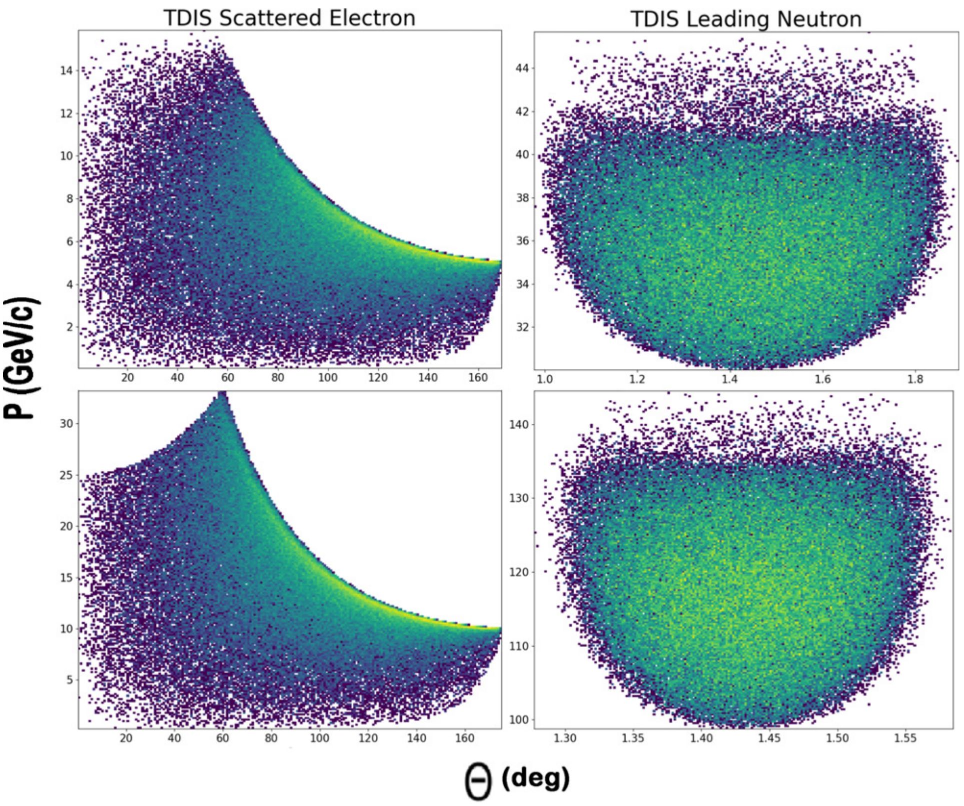

**Figure 11.** A comparison of the scattered electron (left) and leading neutron (right) kinematics for two energy settings: 10 × 135 (bottom) and 5 × 41 (top). The momentum, $P$, and angle, $\theta$, are defined in the lab frame. In both cases, the scattered electrons are within the acceptance of the central detector and the leading neutrons are at small forward angles and carry most of the proton beam energy after the scattering process.

Apparatus for Meson and Baryon Experimental Research (AMBER) will play a crucial role, as they can uniquely provide pionic (kaonic) Drell–Yan measurements in the CM energy region of ∼10–20 GeV [175]. Some older pionc and kaonic Drell–Yan measurements exist, but for the kaon, these are limited to less than 10 data points worldwide, so these measurements are essential for a global effort aimed at pion structure function measurements (also providing a handle on the determination of the so-called 'pion flux' for EIC Sullivan process measurements) and a *sine qua non* for any kaon structure function data map. The AMBER data, in themselves, will already offer new fundamental insights into the emergent hadron mass mechanism.

An electron–ion collider in China (EicC) is under consideration with a similar CM energy range to that of AMBER (∼ 10–20 GeV) and bridging the energy range between the Jefferson Lab and EIC [176]. EicC on its own, and even more, in combination with AMBER, can provide good access to the region $x \gtrsim 0.01$ for pion, and especially kaon, structural function determination and the impact of emergent hadron mass mechanisms on valence quark and gluon structure. In addition, EicC can extend the Rosenbluth L/T-separated cross-section technique beyond Jefferson Lab and access pion and kaon form factors at higher $Q^2$ values, perhaps by a factor of two to four.

The EIC, with its larger CM energy range, will clearly have the final word on the contributions of gluons in pions and kaons, as compared to protons. It will finally settle questions

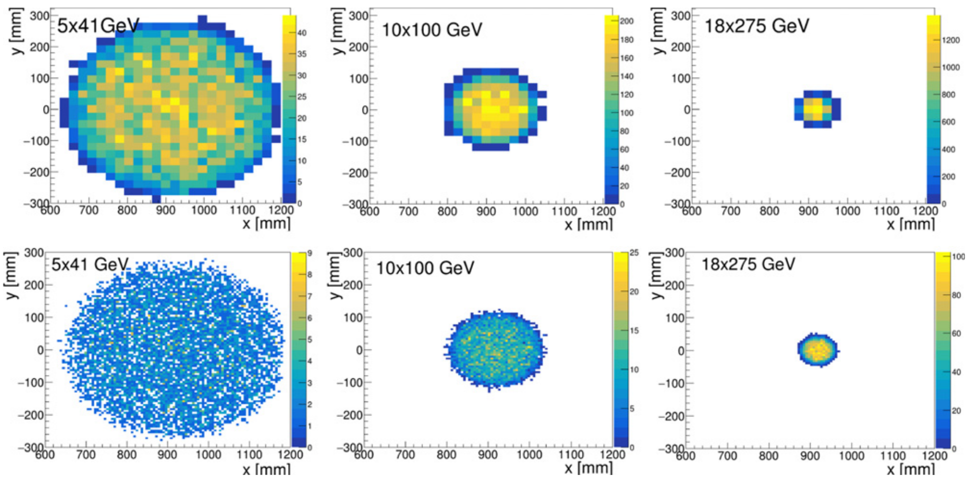

**Figure 12.** Acceptance plot for neutrons in the 60 × 60 $\text{cm}^2$ ZDC, with a low spatial resolution of 3 cm (upper panels) and with a high spatial resolution of 0.6 cm (lower panels), for different energy settings, from left to right, of 5 × 41, 10 × 100, and 18 × 275. The acceptance plot for 5 × 100 would be similar to that shown for 10 × 100. The lower proton (ion) energies set the requirement for the size of the ZDC, whereas the higher proton (ion) energies drive the spatial resolution requirement.

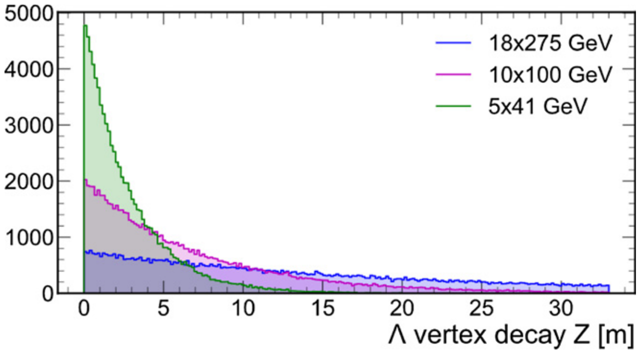

**Figure 13.** The Λ-decay spectrum along the beamline for different beam energies.

**Table 2.** Percentage of decayed Λ's at different detection ranges.

| $E_{\text{beams}}$ | $Z_{\text{vtx}} < 5$ m | 5 m $< Z_{\text{vtx}} < 30$ m | $Z_{\text{vtx}} > 30$ m |
|---|---|---|---|
| 5 × 41 | 83.0% | 16.6% | 0.4% |
| 10 × 100 | 52.1% | 46.7% | 1.2% |
| 18 × 275 | 23.3% | 56.2% | 20.5% |

relating to the gluon content of Nature's NG modes when they are viewed with very high resolution, and vastly extend the $(x, Q^2)$ range of pion and kaon charts and meson structural knowledge.

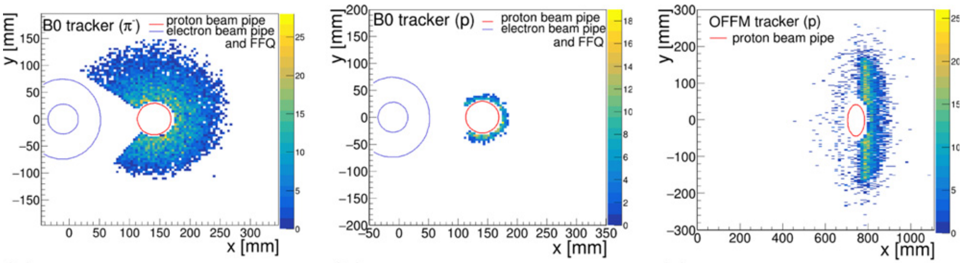

(a) (b) (c)

**Figure 14.** Occupancy plots for the energy setting 5 × 41 (a) for $\pi^-$ in the B0 tracker, (b) for protons in the B0 tracker and (c) for protons in the off-momentum detectors. The red circle shows the beam pipe position and the blue circle shows the electron final-focus quadrupole (FFQ) aperture inside the B0 dipole.

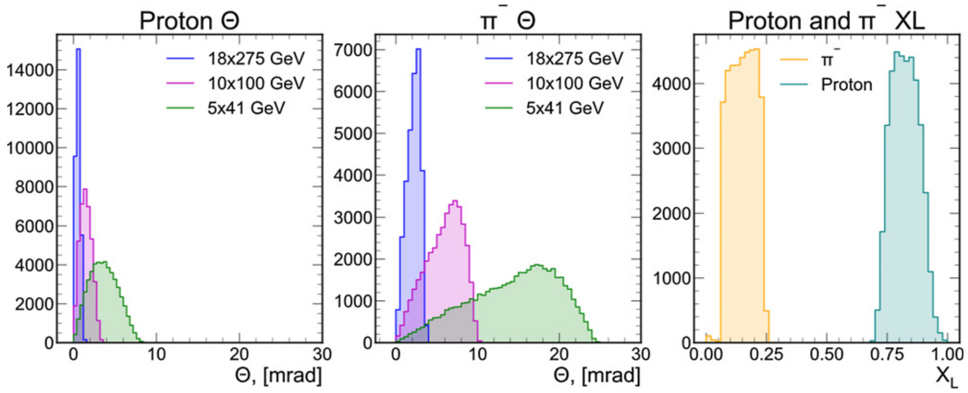

**Figure 15.** Theta and $x_L$ distributions for the detected decay products of $\Lambda$ particles for different beam energy combinations. Proton theta (left), $\pi^-$ theta (centre), proton and $\pi^- X_L$ (right).

## 4. Kinematic coverage and detector requirements

### 4.1. *Far-forward area setup*

The far-forward EIC detector is described in detail in the EIC Yellow Report [165]. Figure 10 shows the main elements of this far-forward region. For the detection of particles of relevance to meson structural studies, all sub-components of the far-forward area play an important role: detection in the B0 area, detection of decay products by off-momentum detectors, and detection of forward-going protons and neutrons by the Roman pots and the zero-degree calorimeter (ZDC).

### 4.2. $e\,p \rightarrow e' + X + n$

The initial pion structural studies were conducted at the highest energy of 18 × 275 (corresponding to the electron and proton beam energies, respectively, both in GeV) to maximise the kinematics coverage. However, to improve access to the high $x_\pi$ region, alternate lower beam energies of 10 × 135 and 5 × 41 were also selected. These lower beam energies allow access to this high $x_\pi$ regime over a wider range of $Q^2$. For a comparison, the 18 × 275

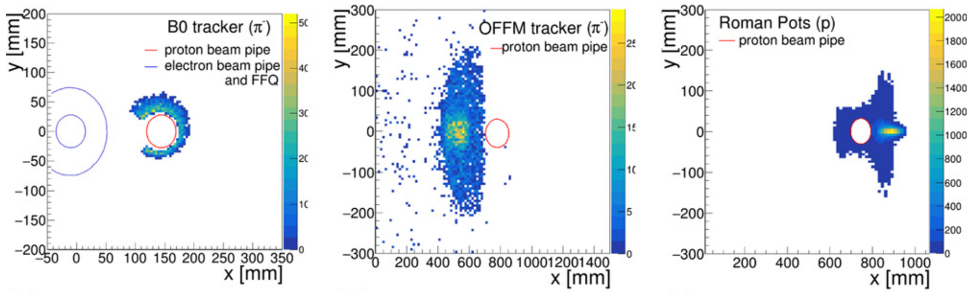

(a) (b) (c)

**Figure 16.** Occupancy plots for the energy setting 10 × 100 (a) for $\pi^-$ in the B0 tracker, (b) for $\pi^-$ in the off-momentum tracker, and (c) for protons in the Roman pot detectors. The red circle shows the beam pipe position and the blue circle shows the electron FFQ aperture inside the B0 dipole.

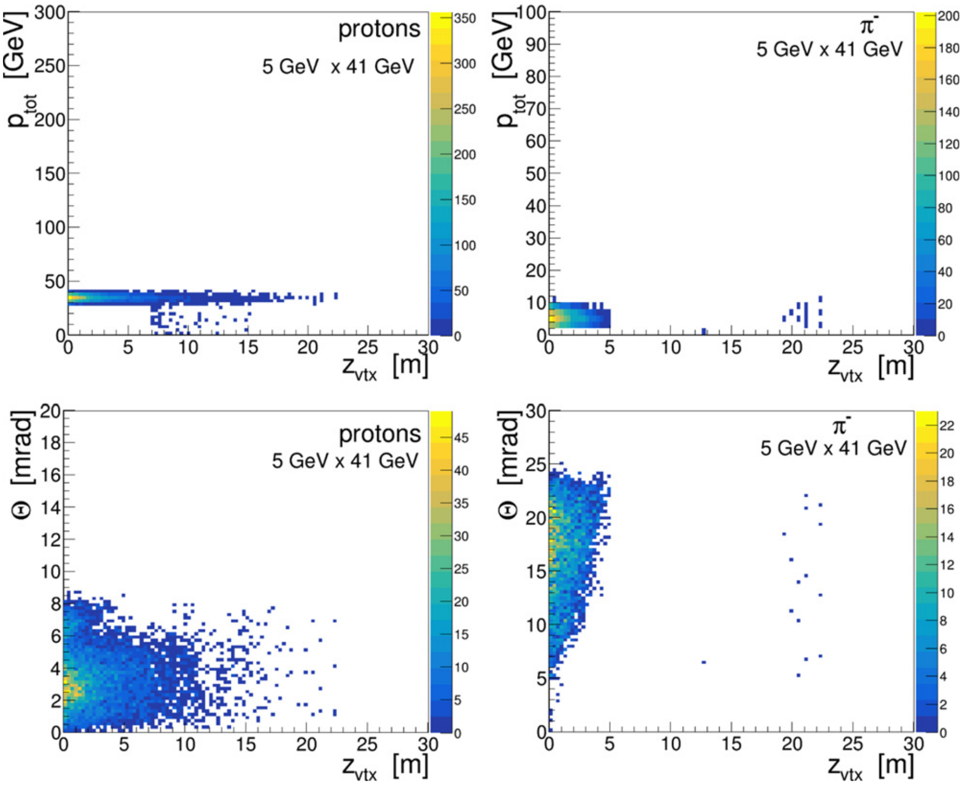

**Figure 17.** Momentum (top) and angular (bottom) distributions of protons (left) and $\pi^-$ (right) from the $\Lambda \rightarrow p + \pi^-$ decay at the beam-energy setting 5 × 41, as registered by the far-forward detectors as a function of their origin (the decay vertex).

energies allow access to high $x_\pi$ data over a $Q^2$ range of $\sim$200–1000 GeV$^2$, while at the 10 × 135 energies, that range was increased to $\sim$30–1000 GeV$^2$, and at the 5 × 41 energies, it was $\sim$5–1000 GeV$^2$. The lower-energy combination of 5 × 41 is even more beneficial for tagging kaon structure by allowing detection of the leading $\Lambda$ events.

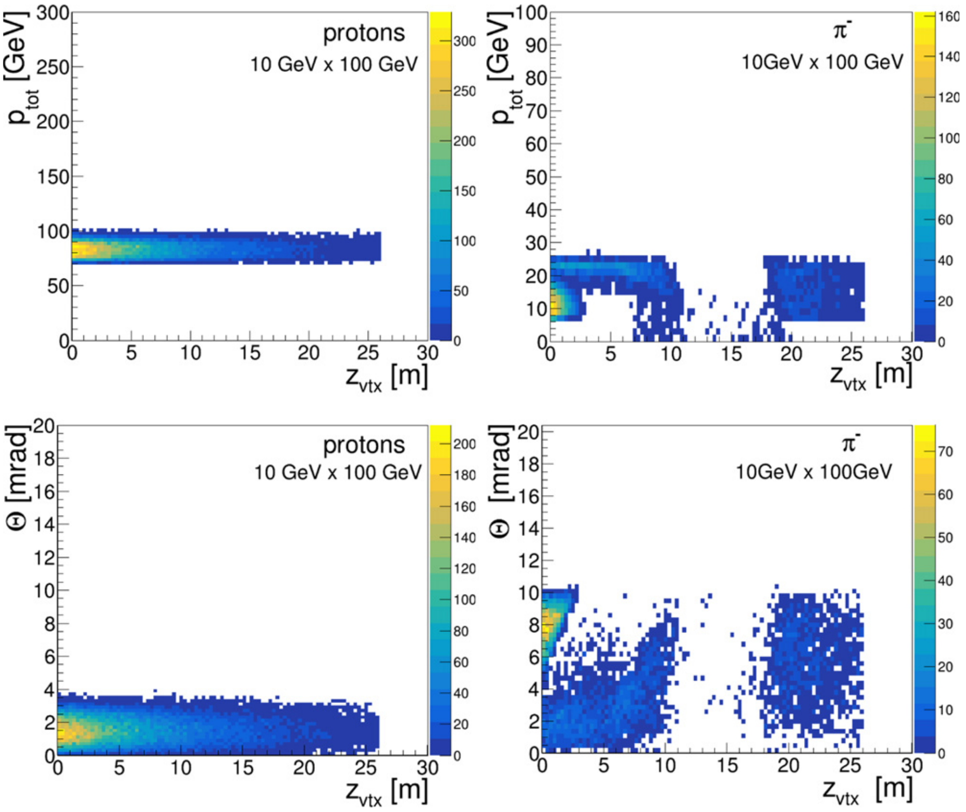

**Figure 18.** Momentum (top) and angular (bottom) distributions of protons (left) and $\pi^-$ (right) from the $\Lambda \to p + \pi^-$ decay at the beam-energy setting 10 × 100, as registered in the far-forward detectors as a function of their origin (the decay vertex). For the $\pi^-$, one clearly sees the 'dead' area in the FFQ magnet region where the placement of detectors is impossible.

The kinematics for the more advantageous lower energy settings, 10 × 135 and 5 × 41, are shown in figure 11. While the scattered electrons are within the acceptance of the central detector, the leading neutrons for these two energy settings are at a very small forward angle while carrying nearly all of the proton beam momentum. These leading neutrons are detected by the ZDC.

Figure 12 shows the acceptance plots for neutrons in the ZDC for all three energy settings. As can be seen, the spatial resolution of the ZDC plays an important role at the highest energy setting, since it is directly related to the measurements of $p_T$ or $t$. For the lowest energy setting, the total acceptance coverage of the ZDC is important. This sets a requirement for the total size of ZDC to be a minimum of 60 × 60 cm$^2$. Such a configuration of the ZDC provides nearly 100% neutron detection efficiency for this channel.

### 4.3. $\Lambda$ tagging

For the case of a leading $\Lambda$ event, due to elastic or DIS scattering from a kaon, both $\Lambda$ decay products must be detected at small forward angles owing to the nature of two-body decay kinematics. The detection of these decay products requires high resolution and granularity because of the small angle of separation of the decay products.

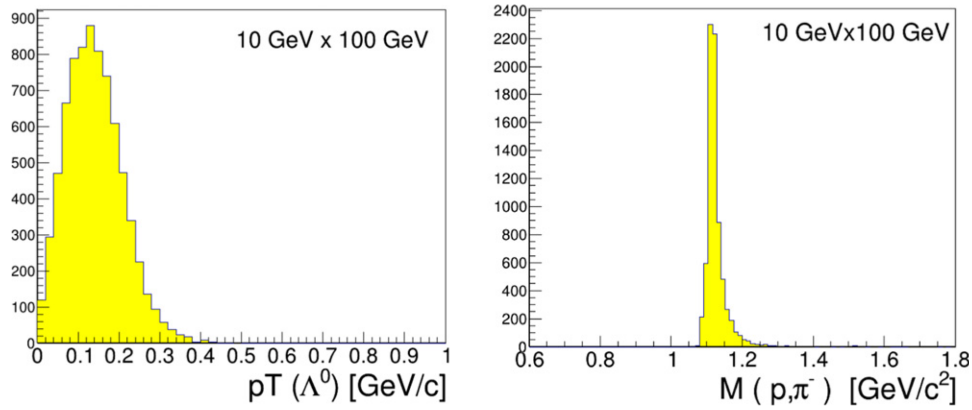

**Figure 19.** $p_{\mathrm{T}}$ (left) and invariant mass (right) of reconstructed $\Lambda$ particles for the $10 \times 100$ beam energy setting.

Detection of the decay channel $\Lambda \rightarrow n + \pi^0$ is feasible, but will require electromagnetic calorimetry before the ZDC to distinguish the neutron and the two photons generated by $\pi^0$ decay. Detection of the other decay channel, $\Lambda \rightarrow p + \pi^-$, poses a greater instrumentation challenge due to its requirement for additional charged-particle trackers or a veto trigger on the path to the ZDC.

The reconstruction of the $\Lambda$ event in the far-forward detection area is one of the most challenging tasks. This is mainly due to the fact that these leading $\Lambda$s have an energy that is close to the initial beam energy, and thus their decay lengths can be tens of metres along the $Z$-axis (or beamline). This complicates the detection of the decay products and hence, the final $\Lambda$ mass reconstruction.

Figure 13 illustrates this further, showing the $Z$-coordinates of the $\Lambda$-decay location for different beam energies. For the lower beam-energy settings ($5 \times 41$), most $\Lambda$ decays are within the central detector region, but at the higher proton (ion) beam energies, the $\Lambda$ decays happen more in the forward-detection area, and the tails of the decay process nearly reach the ZDC's location. Table 2 shows the percentage of decayed $\Lambda$ for different energies and different $Z$ ranges: $Z_{\mathrm{vtx}} < 5$ m, 5 m $< Z_{\mathrm{vtx}} < 30$ m, and $Z_{\mathrm{vtx}} > 30$ m.

To study the possibility of $\Lambda$ mass reconstruction further, both of the main decay modes have been examined: $\Lambda \rightarrow p + \pi^-$, with a branching ratio of 63.9%, and $\Lambda \rightarrow n + \pi^0$, with a branching ratio of 35.8%. The two channels can be cleanly separated by the different charges of the final-state particles, and thus by the different detector components that will play a role in their detection.

### *4.3.1.* $\Lambda \rightarrow p + \pi^-$.

For this process, there are only charged particles in the final state. Therefore, one must rely on subcomponents in the far-forward area, such as the B0 tracker, the off-momentum trackers, and Roman pots for the detection and reconstruction of the decay products.

As an example, occupancy plots for the beam-energy setting of $5 \times 41$ are shown in figure 14. Since this is the lowest beam-energy setting, most of the $\Lambda$s decay in the first metre (before the B0 magnet), and the $\Lambda$ decay products are expected to have low momenta. Therefore, as expected, protons coming from the $\Lambda$ decays will mostly be detected, owing to their lower rigidity, in the off-momentum detectors (c) and partially in a B0 tracker (b). For pions, on the other hand, the tracker inside the B0 dipole is the only detecting element (a). As one

**Table 3.** $\Lambda$ detection efficiency as a function of energy setting, for $\Lambda$ detection with an cut of $Z_{\mathrm{vtx}}$ applied to decay $< 4$ m to ensure $\Lambda$-mass reconstruction.

| Beam energy | $5 \times 41$ | $10 \times 100$ | $18 \times 275$ |
|---|---|---|---|
| Lambda efficiency | 20% | 15% | 1% |

can also see from this figure, the proton-beam-pipe aperture inside the B0 dipole plays an important role and determines the detection efficiency for pions, as well as the azimuthal angle $\phi$-coverage of the detecting elements around the proton beam pipe. Further information on the distributions of the detected decay products at these lower beam energies of $5 \times 41$ are given in figure 15.

For the higher beam-energy settings, e.g. $10 \times 100$, the protons are detected by the roman pots (and partially by the off-momentum detectors); see figure 16. Pions originating from a $\Lambda$-decay with $Z_{\mathrm{vxt}} < 4$ m will only be partially detected in the B0 area, while most of them will go undetected through the proton beam pipe. Pions with higher momentums and lower angles ($p_t$ or theta) can pass through the bores of the FFQs and be detected in the off-momentum detectors. Their detection represents the denser (less dense) area of detection in the off-momentum detectors (figure 16(b)). Note that owing to the negative charge of the pions, they will experience an opposite curved path in the dipoles, compared to protons (compare them with the protons in the off-momentum detectors in figure 14(b)). Therefore, in order to detect the $\Lambda$-decays in this channel, the off-momentum detectors need to provide full azimuthal coverage, to establish appropriate detection for the negatively-charged particles.

For the $5 \times 41$ beam-energy combination, figure 17 shows the momentum (top panels) and angular (bottom panels) distributions of protons (left panels) and pions (right panels) produced by $\Lambda$-decay as a function of distance from the $\Lambda$-decay point, as detected in one of the beamline sub-detectors. This in turn illustrates which of the sub-detectors along the beamline detects the decay products. The protons carry most of the initial proton beam momentum and extend over the far-forward area, with angles of less than 8 mrad. On the other hand, as one can clearly see from the high density of hits, the $\Lambda$-reconstruction efficiency mainly depends on the efficiency of pion detection in the B0 area, with angles in the 5–25 mrad range.

For the higher beam-energy combination, for example $10 \times 100$, the situation is very different. Figure 18) shows the momentum and angular distributions for protons and $\pi^-$. For the latter, one can clearly see a 'dead' area appear along the beamline, where the FFQ beam elements are located, prohibiting the placement of detectors and thus $\pi^-$ detection. This is due to the fact that these pions have significantly lower momentum and so are swept into the magnets and beamline. Those $\Lambda$s that decay beyond the set of FFQs are tagged by the off-momentum detector, but since their $Z_{\mathrm{vtx}}$ is unknown, it is difficult to make a one-to-one correlation between the tagged position and the particle's momentum or angle. Therefore, for the final reconstruction of the $\Lambda$ invariant mass, one has to only use events with $Z_{\mathrm{vtx}} < 3$–5 m, to make this correlation possible. That this remains possible is revealed in figure 19(right), which shows the invariant mass spectra of the $\Lambda(p, \pi^-)$ channel for this $10 \times 100$ beam-energy setting. The corresponding $p_{\mathrm{T}}$ spectrum of the $\Lambda$ particles is shown in the left panel of figure 19.

We summarise this result in table 3, which shows the expected $\Lambda$ detection efficiency for the decay $\Lambda \to p + \pi^-$. A cut on decay within 4 m, $Z_{\mathrm{vtx}} < 4$ m has been applied for this selection. The decrease in detection efficiency for the higher-energy settings mainly originates from this $Z_{\mathrm{vtx}}$ cut, but is necessary to ensure $\Lambda$ mass reconstruction.

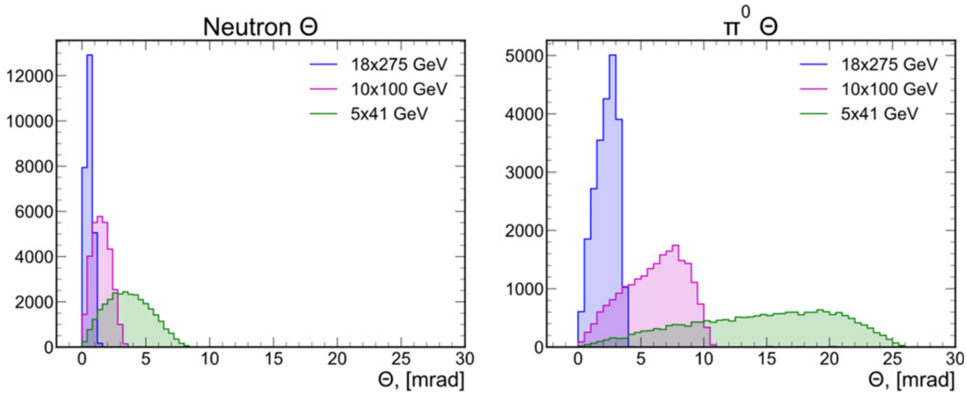

**Figure 20.** Angular distributions for detected decay products of $\Lambda \rightarrow n + \pi^0$: (a) neutrons; and (b) $\pi^0$. Beam energy settings: 18 × 275, 10 × 100, and 5 × 41.

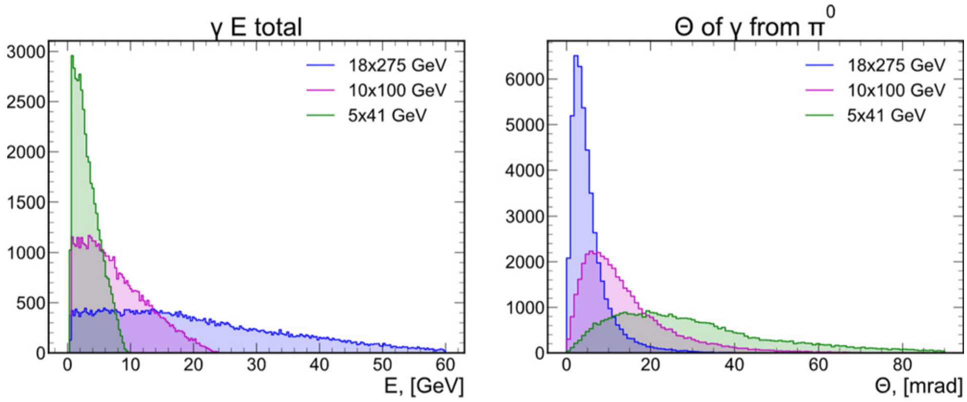

**Figure 21.** Energy and angular Θ distributions for the detected $\gamma\gamma$ used to reconstruct the $\pi^0$ from a $\Lambda$ decay channel.

*4.3.2.* $\Lambda \rightarrow n + \pi^{\circ}$. For this process, there are only neutral particles in the final state. The main detection scheme for these particles is the ZDC and/or some kind of electromagnetic calorimeter/photon detector in the B0 area. As with the $p + \pi^-$ decay mode, with lower beam energies, more particles can be detected in the central detector region. Figure 20 shows the angular (Θ) distributions for $n$ and $\pi^0$ for different beam energies. It is furthermore assumed that the $\pi^0$ is reconstructed from $\pi^0 \rightarrow \gamma\gamma$, where the photons are deposited in one of the corresponding detectors.

The energetic and angular distributions of the two photons from the $\pi^0$ decay are shown in figure 21, for various beam-energy settings. At lower-beam energy settings, some measurement to detect the larger-angle photons in the B0 area is required to recapture efficiency. As the beam energy increases, the ZDC starts playing the main role for the detection of both neutrons and neutral pions. This is illustrated further in figure 22, which shows the occupancy plots of the ZDC for both neutrons and the $\gamma\gamma$ from $\pi^0$ decay for different energy settings. At the higher 10 × 135 energies, the ZDC captures all photons from neutral pion decay, while at the lower 5 × 41 energies, many photons are at larger angles, thereby reducing the fraction detected in the ZDC.

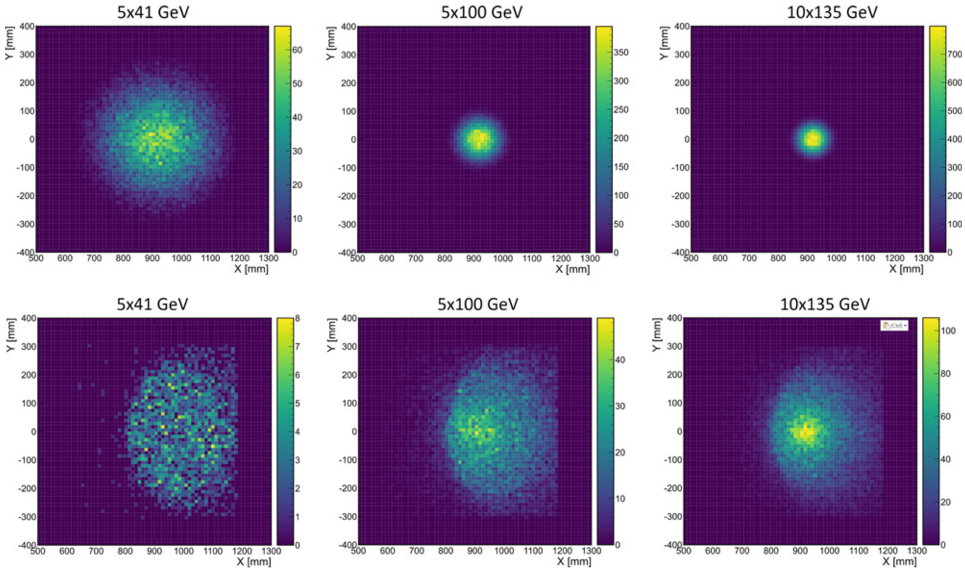

**Figure 22.** Occupancy distribution for neutrons (top panels) and $\gamma\gamma$ from $\pi^0$ decay (bottom panels), as detected in the ZDC for different beam energy settings.

### 4.4. Exclusive $p(e, e'\pi^+n)$ events

The kinematic distributions for exclusive $p(e, e'\pi^+n)$ events are shown in figure 23. Similarly to tagged DIS events, the neutrons assume nearly all of the proton beam momentum, and need to be detected at very forward angles in the ZDC. The scattered electrons and pions also have similar momenta to those of the tagged DIS case, except that here, the electrons are distributed over a wider range of angles. For instance, at the 5 × 100 beam-energy setting, the 5–6 GeV electrons are primarily scattered at 25–45° from the electron beam, while the 5–12 GeV $\pi^+$ electrons are scattered at 7–30° from the proton beam. Further details of the exclusive events study, including the assumed requirement to separate exclusive events from the non-exclusive background, and the pion form-factor projections, are given in section 5.2.

### 4.5. Accelerator and instrumentation requirements

The physics simulation examples show that access to the meson structure benefits greatly from EIC operations at the lower center-of-mass energies, with both ep and ed measurements at similar CM energies. Lower energies enhance the range of $Q^2$ at large $x_\pi$. Lower energies allow detection to uniquely tag the kaon structure: this enhances $\Lambda$ decay probability at short distances and permits $\Lambda$-mass reconstruction to work from the detected decay products. To tag the meson structure, proper instrumentation of B0 tracking detectors is needed, with full azimuthal coverage and perhaps a smaller proton-beam pipe diameter. Off-momentum detectors also have to provide full azimuthal coverage to detect negatively-charged decay particles.

In terms of complimentarity, an improved spectrometer along the beamline would be beneficial to enhance the efficiency of detection of low-momentum decay particles. The present beamline design leaves a large area with no possible detection, making $\Lambda$ tagging difficult for particles originating from larger $Z_{\rm vtx}$. This complicates access to the meson structure at larger proton (ion) beam energies. Alternatively, a beamline design with an improved secondary focus could be beneficial for $\Lambda$ tagging.

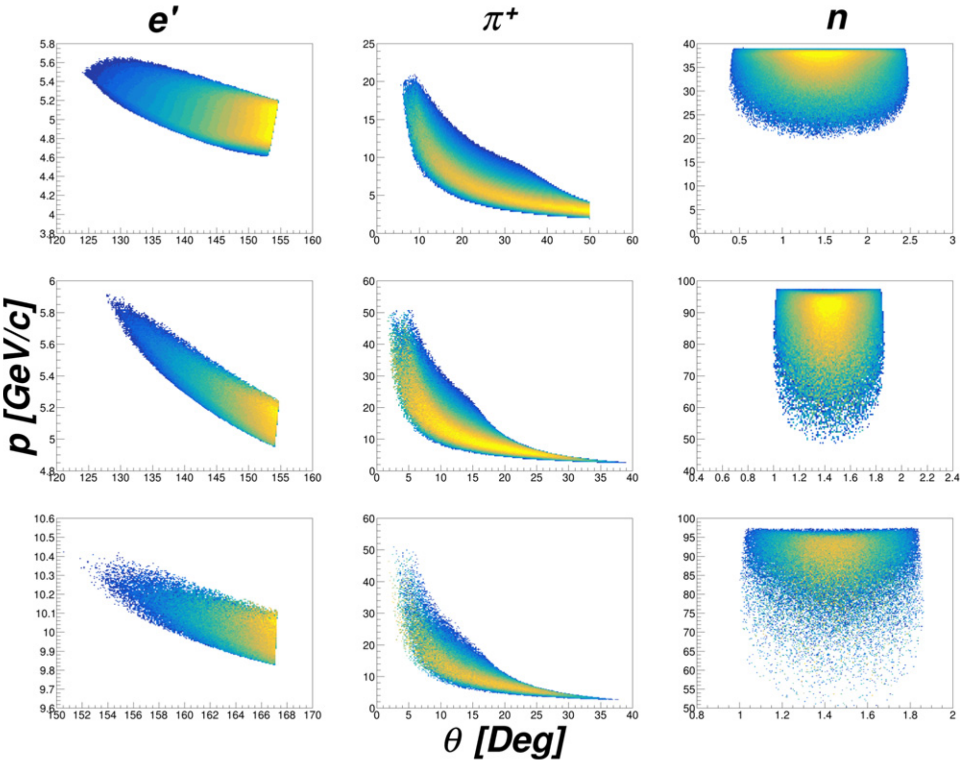

**Figure 23.** Kinematic distributions for exclusive $p(e, e^{\prime}\pi^{+}n)$ events for $e^{\prime}$ (left), $\pi^{+}$ (centre), and $n$ (right), at $5 \times 41$ (top), $5 \times 100$ (middle), and $10 \times 100$ (bottom) beam energies. The neutron distribution is offset by 25 mrad owing to the beam crossing angle.

## 5. Physics projections

### 5.1. Meson structure functions

*5.1.1. Pion structure function projections.* A fast Monte Carlo was used for feasibility studies of the $\pi$ and $K$ structural function measurements. The Monte Carlo is a C++ and Object Oriented Data Analysis Framework (ROOT)-based custom event generator [177] that uses the random number generator TRandom3 in ROOT. The inputs of the generator are the minimum and maximum $Q^2$ and $x$ values, the initial ion and electron beam energies, flags for initial beam smearing, and the number of events to simulate. The generator uses various quantities such as the CTEQ6 PDF tables, nucleon structure functions, and the tagged $\pi$ and $K$ structural functions and splitting functions. The $\pi$ structure function, in particular, can be parametrised in many ways. Here, the $F_2^{\pi}$ structure function is calculated at NLO through the use of pion PDFs, which were determined in [144].

The hadronic splitting function, $\mathsf{f}_i$, that appears in equation (10) determines the meson flux that is essential to computing the leading-baryon production cross-section of equation (9). For the sake of the simulations presented in this analysis, this flux was computed in the context of the single-meson exchange framework, which is valid for soft exchange momenta. The details of the hadronic splitting function were fixed to the relativistic vertex factor approach used in [142], including a $s_{\pi N}$-dependent Gaussian interaction with the ultraviolet regulator

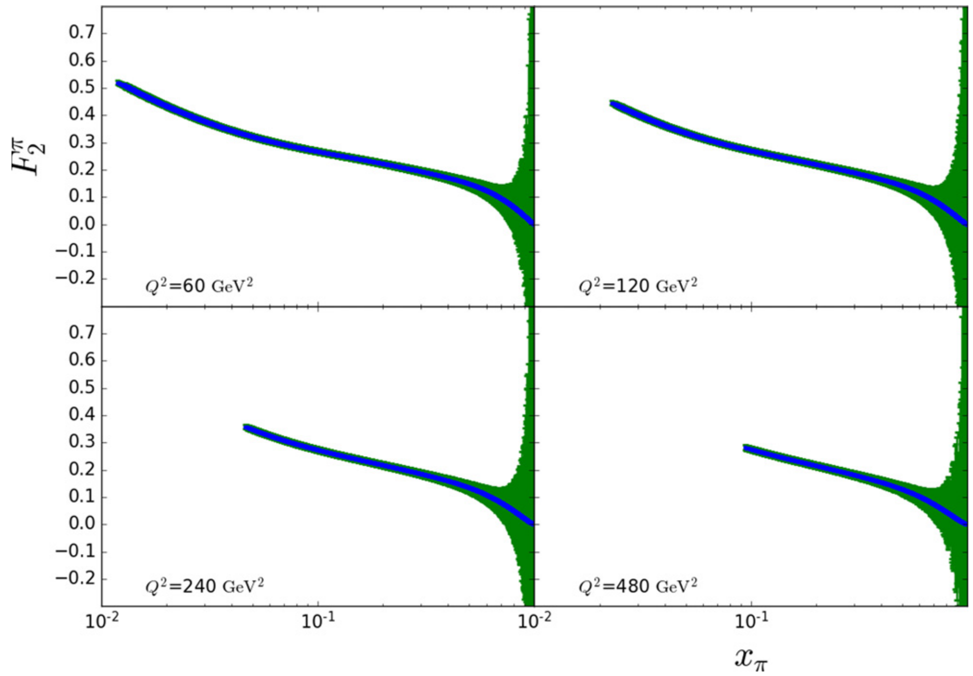

**Figure 24.** Monte Carlo projections of the pion structural function vs $x$ for a beam energy of $10 \times 135$. The projected data are binned in $x$ and $Q^2$, with bin sizes of 0.001 and 10 GeV$^2$, respectively. The blue points are the Monte Carlo projections for $Q^2$ values of 60, 120, 240, 480 GeV$^2$/c. The green bands are the statistical uncertainties for a luminosity of 100 fb$^{-1}$.

$\Lambda \sim 1$ GeV. Although the details of the hadronic splitting were not varied while simulating the EIC tagging measurements, it should be stressed that the EIC can be expected to be sensitive to the meson flux as well as the meson structural function. A detailed examination of the sensitivity to the meson flux will be undertaken in the future.

The plot in figure 24 shows the reach in $x$ for four $Q^2$ bins at the $10 \times 135$ energy setting. The pion structural function simulations were validated by their agreement with the experimental HERA data [126] in that regime, and with the Glueck, Reya, Vogt (GRV) fit [122] at higher $x$. Statistical uncertainties with the addition of the leading neutron detection fraction (discussed in the previous section) were incorporated to the overall uncertainty for a luminosity of $\mathcal{L} = 100$ fb$^{-1}$. For this energy, the coverage in $x$ extends down to $10^{-2}$, with reasonable uncertainties in the mid-to-large $x$ region, increasing rapidly as $x \to 1$. Even with these restrictions, the coverage in mid-to-high $x$ is unprecedented, and should allow for detailed comparisons between the pion and kaon structures.

In figure 7, we showed the impact of EIC data on the pion PDFs themselves and their uncertainties, folding in the estimated systematic uncertainty and the projected statistical uncertainties from the simulations (see figure 8). The resulting access to a significant range of $Q^2$ and $x$, for appropriately small $-t$, will allow for much-improved insights into the gluonic content of the pion.

Figure 25 displays the ratio of the uncertainty of the $F_2^\pi(x_\pi, Q^2)$ structural function resulting from a global fit with the projected EIC data to that without it. We show various $Q^2$ values over a wide range between a few GeV$^2$ and a few hundred GeV$^2$ over the range $10^{-3} < x_\pi < 1$ to

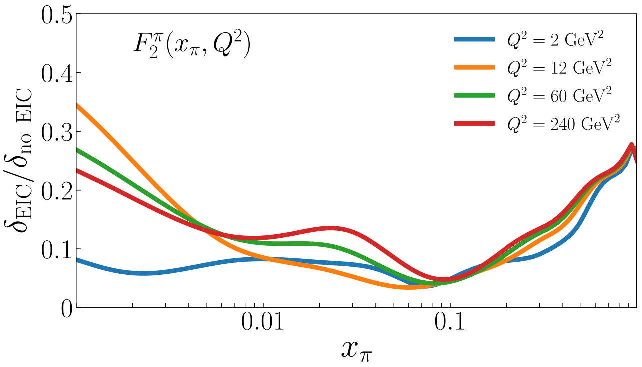

**Figure 25.** Ratio of the uncertainty of the $F_2^\pi$ structural function from the global fit with and without the inclusion of EIC projected data to the uncertainty of the $F_2^\pi$ as a function of $x_\pi$ for various $Q^2$ values.

investigate the $Q^2$ dependence of the impact. Strikingly, the $F_2^\pi$ structural function's uncertainties are reduced by 80%–90% in the range of $x_\pi$ between $3 \times 10^{-3}$ and 0.4 in the presence of the EIC data, regardless of the values of $Q^2$. Within the whole range, the uncertainties are reduced by 65% or more. Below an $x_\pi$ of 0.1, the $F_2^\pi$ structural function is reduced by a factor of 10 for the case when $Q^2 = 2$ GeV$^2$. The constraining power at such low values of $Q^2$ is illustrated in figure 8, where all data points shown are in the range $Q^2 < 10$ GeV$^2$. The EIC provides a unique opportunity to improve our knowledge of the $F_2^\pi$ over a large range in $Q^2$ and $x$.

As discussed in section 3.1, theoretical calculations [44] predict that the Sullivan process should provide clean access to the meson structure below a minimum value of $-t$. For the pion, this is $-t \leqslant 0.6$ GeV$^2$. Similarly, corrections to extract the pion's structural information from the theoretical backgrounds (absorptive corrections, higher meson-mass exchanges, etc., see section 3.2) are minimized by measuring at the lowest $-t$ possible. Experimentally, this can be addressed by various tagged pion structural measurements as a function of $-t$, for low $-t <\sim 0.6$ GeV$^2$al, and by verifying the pion structural extraction.

Figure 26 shows the reduction of the uncertainties of the four-fold differential cross-section, $\frac{\mathrm{d}^4\sigma}{\mathrm{d}x\, dQ^2\, \mathrm{d}x_L\, \mathrm{d}t}$. The impact is illustrated by means of the ratio of cross-sections, including the EIC projected data, to the uncertainty of that without the EIC, as a function of $-t$ and up to $-t = 1$. The left and middle panels of figure 26, show that as a function of $-t$, the uncertainties on the differential cross section are reduced by 90% at $x = 0.001$ and $x = 0.01$. For the case whereby $x = 0.1$ in the right panel, the values of $Q^2$ are insignificant in the ratio of uncertainties. At large $Q^2$, at $x \sim 0.1$, the ratio of uncertainties rises when $-t$ is closer to 0, due to a reduced experimental phase space in the low $-t$ region for those kinematics. The overall impact of the $>75\%$ improvement in the uncertainties indicates both that our knowledge is currently poor and that the EIC will provide good constraints for cross-sections. Furthermore, this underlines that the measured tagged cross-sections as function of $-t$ can be used to confirm the robustness of pion structural extraction.

*5.1.2. Kaon structure function and splitting function projections.* The pion structural function analysis presented here can be extended to the kaon, as the single-meson exchange framework can be generalised to the flavour SU(3) sector with expected validity for soft-exchange kaons. Empirical knowledge of the kaon sector is even more sparse than the analogous information for the pion. As such, comprehensive data would be of great utility for unravelling the splitting

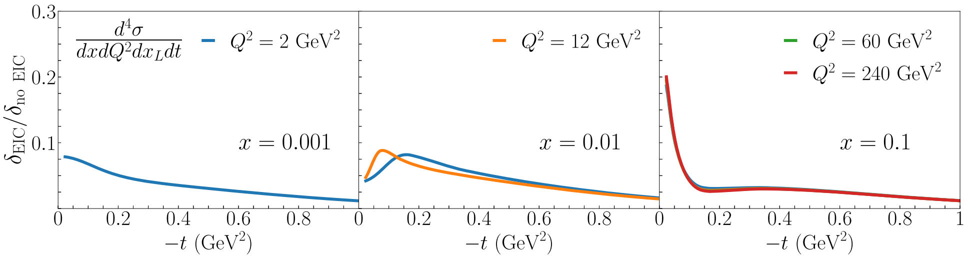

**Figure 26.** Ratios of the uncertainty of the differential cross-section $\frac{\mathrm{d}^4\sigma}{\mathrm{d}x\,\mathrm{d}Q^2\,\mathrm{d}x_L\,\mathrm{d}t}$ from the global fit including EIC projected data to the uncertainty of that without the EIC data as a function of $-t \in [-t_{\rm min}, 1]$ for various $Q^2$ and for (left panel) $x = 0.001$, (middle panel) $x = 0.01$, and (right panel) $x = 0.1$. For all calculations, the value $x_{\rm L} = 0.85$ was used.

function ratio, $\mathsf{f}_K/\mathsf{f}_\pi$ as well as the structural function of the kaon, $F_2^K$. For initial simulations, the splitting function $\mathsf{f}_K$ might be fixed at the first order to inclusive hadroproduction data, and $\Lambda$(uds) baryon production according to equation (9). Ultimately, precise EIC data over a range of $x$, $Q^2$, $y$, and $t$ would be instrumental for unravelling and constraining the meson flux model from the structural function $F_2^K$.

### 5.2. *Meson form factors*

The experimental determination of the $\pi^+$ electric form factor ($F_\pi$) is challenging. The best way to determine $F_\pi$ would be electron–pion elastic scattering. However, the lifetime of the $\pi^+$ is only 26.0 ns. Since $\pi^+$ targets are impossible and $\pi^+$ beams with the required properties are not yet available for measurements at modest-to-large $Q^2$ values, one must employ exclusive electroproduction, $p(e, e'\pi^+)n$. This is best described as quasi-elastic ($t$-channel) scattering of the electron from the virtual $\pi^+$ cloud of the proton, where $t$ is the Mandelstam momentum transferred $t = (p_p - p_n)^2$ to the target nucleon. As discussed in section 3.1, scattering from the $\pi^+$ cloud dominates the longitudinal photon cross-section ($\mathrm{d}\sigma_{\rm L}/\mathrm{d}t$) at sufficiently small $-t$.

To reduce background contributions, one normally separates the components of the cross-section arising from longitudinal (L) and transverse (T) virtual photons (and the LT, TT interference contributions) via a Rosenbluth separation. However, L/T separations are impractical at the EIC, as one cannot reach sufficiently low $\epsilon$ data to provide a good lever arm. Below, we propose an alternate technique to access $\sigma_{\rm L}$ via a model, validated with exclusive $\pi^-/\pi^+$ ratios from deuterium. Once $\mathrm{d}\sigma_{\rm L}/\mathrm{d}t$ has been determined over a range of $-t$, from $-t_{\rm min}$ to $-t \approx 0.6$ GeV$^2$, the value of $F_\pi(Q^2)$ is determined by comparing the observed $\mathrm{d}\sigma_{\rm L}/\mathrm{d}t$ values with the best available electroproduction model, incorporating off-shell pion and recoil nucleon effects. In principle, the obtained $F_\pi$ values depend upon the model used, but one anticipates this dependence to be reduced at sufficiently small $-t$. Measurements over a range of $-t$ are essential as part of the model validation process. The JLab 6 GeV experiments were instrumental in establishing the reliability of this technique up to $Q^2 = 2.45$ GeV$^2$ [24, 39, 40, 178–183], and extensive further tests are planned as part of JLab experiment E12-19-006.

*5.2.1. Requirements for separating exclusive and SIDIS events.* The exclusive $\pi^+$-channel cross-section is several orders of magnitude smaller than the neighbouring SIDIS background; but it is distributed over a much narrower range of kinematics, and this is essential for the separation of exclusive events from the background. The exclusive $p(e, e'\pi^+n)$ reaction is isolated by detecting the forward-going high-momentum neutron, i.e. $e - \pi^+ - n$ triple coincidences. Since the neutron energy resolution is not very good, the neutron hit is used as a tag for exclusive events. The neutron momentum is otherwise unused in the event reconstruction.

Detector effects have been simulated via the following ad hoc smearing functions. The pion and electron angular resolutions were estimated by assuming a 10 $\mu$m position resolution in a cylindrical silicon vertex tracker (comparable with ZEUS), and this Cartesian position uncertainty was propagated to polar coordinates $(\theta, \phi)$. From this, $\delta p = 250\ \mu$rad was conservatively assumed for all angles, for both the electron and the pion. The pion and electron momentum resolutions were estimated from track reconstruction in the magnetic field via the resolution in [184], assuming five positional measurements in a 3 T solenoidal field. To simplify the MC study, $\delta p/p = 2\%$ was conservatively assumed for all angles, for both the electron and the pion. Since the neutron energy resolution in the ZDC is not very good, the neutron hit was used as a tag for deep exclusive meson production (DEMP) events. The neutron momentum was not otherwise used in the event reconstruction. Thus, the missing momentum is calculated as $p_{\text{miss}} = |\vec{p_e} + \vec{p_p} - \vec{p_{e'}} - \vec{p_\pi}|$.

The effectiveness of kinematic cuts to isolate the exclusive $\pi^+$ channel was evaluated by comparison with a simulation of $p(e, e^{'}\pi^+)X$ SIDIS events, including both detector acceptance and resolution smearing effects. The most effective cuts are on the detected neutron angle (±0.7° from the outgoing proton beam), the reconstructed $-t < 0.5$ GeV$^2$, and the missing momentum defined above. The $p_{\text{miss}}$ cut is $Q^2$-bin dependent, where the value is chosen to optimize the signal/background ratio for each bin. It ranges from $p_{\text{miss}} > 95$ GeV/c at $Q^2 = 6$ GeV$^2$, to 77 GeV/c at $Q^2 = 35$ GeV$^2$, where all events are removed above the cut value. After application of these cuts, the exclusive $p(e, e^{'}\pi^+ n)$ events are cleanly separated from the simulated SIDIS events.

**Determining the longitudinal cross-section $\mathbf{d\sigma_L/dt}$.** After the exclusive $\pi^+ n$ event sample is identified, the next step is to separate the longitudinal cross-section, $\mathrm{d}\sigma_{\mathrm{L}}/\mathrm{d}t$, from $\mathrm{d}\sigma_{\mathrm{T}}/\mathrm{d}t$, as needed for the exaction of the pion form factor. However, a conventional Rosenbluth separation is impractical at the EIC owing to the very low proton beam energy required to access $\epsilon < 0.8$. Fortunately, at the high $Q^2$ and $W$ values accessible at the EIC, phenomenological models predict $\sigma_{\mathrm{L}} \gg \sigma_{\mathrm{T}}$ at small $-t$. For example, the Regge-based model in [185] predicts $R = \sigma_{\mathrm{L}}/\sigma_{\mathrm{T}} > 10$ for $Q^2 > 10$ GeV$^2$ and $-t < 0.06$ GeV$^2$, and $R > 25$ for $Q^2 > 25$ GeV$^2$ and $-t < 0.10$ GeV$^2$. Thus, transverse cross-section contributions are expected to be 1.3%–14%, and the ratios become more favourable with increasing $Q^2$ and decreasing $-t$. The most practical choice appears to be to use a model to isolate the dominant $\mathrm{d}\sigma_{\mathrm{L}}/\mathrm{d}t$ from the unseparated cross-section, $\mathrm{d}\sigma_{\mathrm{uns}}/\mathrm{d}t$.

To control the systematic uncertainty associated with the theoretical correction to estimate $\sigma_{\mathrm{L}}$ from $\sigma_{\mathrm{uns}}$, it is very important to confirm the validity of the model used. This can also be done with EIC data, using exclusive $^2\mathrm{H}(e, e^{'}\pi^+ n)n$ and $^2\mathrm{H}(e, e^{'}\pi^- p)p$ data in similar kinematics to the primary $p(e, e^{'}\pi^+ n)$ measurement. The ratio of these cross-sections is

$$R = \frac{\sigma[n(e, e'\pi^- p)]}{\sigma[p(e, e'\pi^+ n)]} = \frac{|A_{\mathrm{V}} - A_{\mathrm{S}}|^2}{|A_{\mathrm{V}} + A_{\mathrm{S}}|^2}, \tag{11}$$

where $A_{\mathrm{V}}$ and $A_{\mathrm{S}}$ are the isovector and isoscalar amplitudes, respectively. Since the pion pole $t$-channel process used for the determination of the pion form factor is purely isovector (owing to $G$-parity conservation), the above ratio will be diluted if $\sigma_{\mathrm{T}}$ is not small or if there are significant non-pole contributions to $\sigma_{\mathrm{L}}$. The comparison of the measured $\pi^-/\pi^+$ ratio with model expectations, therefore, provides an effective means of validating the model used to determine $\sigma_{\mathrm{L}}$ [182, 183]. The same model, now validated, can likely be used to extract the pion form factor from the $\sigma_{\mathrm{uns}}$ data.

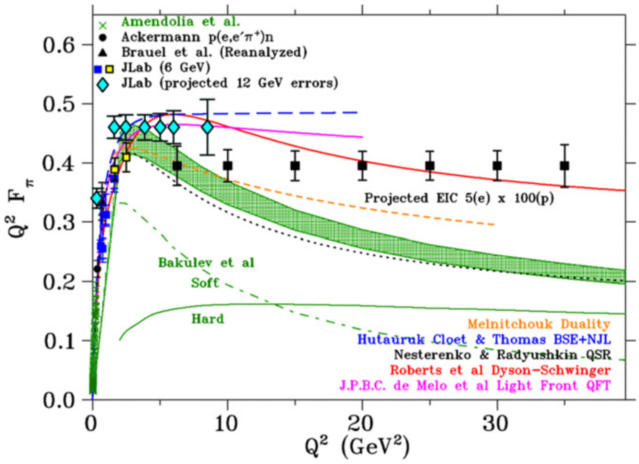

**Figure 27.** Existing data (green [186, 187]; black [40, 188, 189]; blue and yellow [40, 179, 180]) and projected uncertainties for future data on the pion form factor from JLab (cyan [190]) and EIC (black), in comparison to a variety of hadronic structural calculations (orange dash [191]; blue long-dash [131]; black dot [192]; red solid [36]; violet solid [193]; and green [194], where 'hard' means pQCD with analytic running coupling, and the band represents hard + soft, including non-perturbative uncertainties). The EIC projections clearly cover a much larger $Q^2$ range than the JLab measurements. (The magnitudes of the data projections are arbitrary, deliberately expressing no model bias.)

*5.2.2. $\pi^+$ form factor projections.* As already discussed above, the value of $F_\pi(Q^2)$ can be determined by comparing the measured $\sigma_{\text{uns}}$ at small $-t$ to the best available electroproduction model, incorporating pion pole and non-pole contributions and validated with $\pi^-/\pi^+$ data. The model should treat the pion form factor as an adjustable parameter, so that the best-fit value and its uncertainty at fixed $(Q^2, W)$ are obtained by a comparison of the magnitude and $t$-dependences of the model and the data. If several models are available, the form factor values obtained using each one can be compared to better understand the model dependence. The importance of additional $p(e, e'\pi^+n)$ model development to improve the knowledge of pion form factors cannot be overestimated, and additional activity in this area should be encouraged.

Using this technique, the EIC can enable a pion form-factor measurement of up to $Q^2 = 35$ GeV$^2$, as shown in figure 27. Note that the $y$-axis positions of the projected data points in figure 27 are arbitrary. However, the error bars represent the real projected errors for these points. The errors in the yields are based on the following assumptions: cross-sections parametrised from the Regge model in [195], an integrated luminosity of 20 fb$^{-1}$ for $5 \times 100$ GeV measurement, clean identification of exclusive $p(e, e'\pi^+n)$ events by tagging the forward neutron, and a cross-section systematic uncertainty of 2.5% point-to-point and 12% scale. One should then apply the following additional uncertainty, since the form factor will be determined from unseparated, rather than L/T-separated data: $\delta R = R$ systematic uncertainty in the model subtraction to isolate $\sigma_{\text{L}}$, where $R = \sigma_{\text{L}}/\sigma_{\text{T}} = 0.013$–$0.14$ at $-t_{\text{min}}$. The model fitting procedure is finally used to extract $F_\pi(Q^2)$ from the $\sigma_{\text{uns}}$ data, where one assumes the applied model is validated at small $-t$ by comparison to the data. Additional model uncertainties in the form-factor extraction are not estimated here, but the EIC should provide data over a sufficiently large kinematic range to allow the model dependence to be quantified by a detailed analysis.

Forthcoming data at Jefferson Lab [190] will cover the region in $Q^2$ that transitions from a pion form-factor description at large distances to short-distance QCD phenomena, i.e., up to

$Q^2 = 8.5$ GeV$^2$. The pion form-factor projected data at an EIC can extend this by a factor of $\sim$4 and act as a sensitive probe of the magnitude of the pion form factor and a witness of the expected onset of logarithmic decrease. In a fully consistent calculation computed using two different QCD effective charges, a variation of $\approx$20% of the magnitude of the pion form factor was obtained at $Q^2 \sim 5$–10 GeV$^2$ [13]. Evidently, the projected pion form-factor data at the EIC are a sensitive probe of the strength of emergent mass generation.

*5.2.3. $K^+$ form factor.* The reliability of the electroproduction method for determining the $K^+$ form factor is not yet fully established. A recent extraction of the kaon form factor from electroproduction data for $Q^2 = 1.00$–$2.35$ GeV$^2$ is discussed in [196]. L/T separated kaon electroproduction cross-sections were extracted at different values of $-t$ using data from JLab [179, 197, 198] and the successful method described in [179, 181] was applied to determine the kaon form factor. JLab E12-09-011 [43] acquired data for the $p(e,e'K^+)\Lambda$, $p(e,e'K^+)\Sigma^0$ reactions at hadronic invariant mass $W = \sqrt{(p_K + p_{\Lambda,\Sigma})^2} > 2.5$ GeV, to search for evidence of scattering from the proton's 'kaon cloud'. The data are still being analysed, with L/T-separated cross-sections of up to $Q^2 = 5.5$ GeV$^2$ expected in the next $\sim$ 2 years.

If the anticipated data confirm that the scattering from the virtual $K^+$ in the nucleon dominates at low four-momentum transfer to the target $|t| \ll m_p^2$, the experiment will have yielded the world's first quality data for $F_K$ above $Q^2 > 0.2$ GeV$^2$. This would then open up the possibility of using exclusive reactions to determine the $K^+$ form factor over a wide range of $Q^2$ at higher energies. While the general technique will remain the same, the $\pi^-/\pi^+$ validation technique used to confirm the $\sigma_{\rm L}$ extraction cannot be used for the $K^+$. One possibility could be for $\Lambda/\Sigma^0$ ratios to play a similar role. However, conditions under which the clean separation of these two channels may be possible at the EIC requires further study. These studies are planned for the near future.

It is worth highlighting that in QCD, the difference between the kaon and pion charge form factors is of the scale of 20% at $Q^2 \sim 5$ GeV$^2$ [38] and disappears at asymptotic $Q^2$ as $\ln(Q^2)$. The kaon and pion form factors are also identical in the absence of HB couplings into QCD. Indeed, all differences between these form factors are seeded by such HB couplings. Quality data on the kaon form factor in the realm of $Q^2 \sim 5$ GeV$^2$ and above would be very valuable here.

## 6. Summary and prospects

After more than seventy years, there is now a growing realisation that the first ever discovered mesons hold the keys to our further understanding of the vast bulk of visible mass in the Universe. The pion was the first discovered meson, in 1947 [16], soon followed in the same year by the kaon [17], the first strange particle [199, 200]. These NG bosons would be massless if Nature expressed chiral symmetry simply; and would remain massless in the absence of quark couplings to a HB. Yet, these light pseudoscalar mesons are intimately linked to confinement; their structure is complicated; and their masses, although uncommonly light, are not zero, being generated by constructive interference between an emergent mass mechanism, expressed by DCSB, and the Higgs mechanism. Some 100 MeV of the 494 MeV kaon mass, with its heavier strange quark, or 20%, may be directly attributed to the Higgs mechanism.

The emergence of the bulk of visible mass and its manifestations in the existence and properties of hadrons and nuclei are profound questions that probe the heart of strongly interacting matter. What Nature provided as the properties of pions and kaons, the Standard Model's would-be NG modes, are tell-tales of the emergent hadron mass and structural mechanisms and the required interplay with the Higgs mechanism. For example, the quark and gluon energy contributions to the pion and kaon masses yield information about the balance of these mechanisms, the magnitude and scale-dependence of the pion and kaon form factors inform us about the size and range of the interference between emergent mass and the Higgs mass mechanisms, the pressure distribution and transverse momentum distributions in pions as compared to protons inform us about the universality of the attractive and repulsive forces inside hadrons.

Understanding fundamentally requires a synergistic effort that combines experiment, theory, computing, and phenomenology, with the aim of revealing how the roughly 1 GeV mass scale that characterises atomic nuclei appears and why it has the observed value; why ground-state pseudoscalar mesons are unnaturally light in comparison; and to elucidate the role of the HB in forming hadron properties. Pions, kaons, protons and their counterpart neutrons provide the building blocks of the visible Universe. Their exact QCD substructures have now readily become available by marked progress in theory and computing, and their further understanding will, in turn, shed light on how Nature created mass and visible structure.

The foreseen EIC will be a real game changer for experimental data on the pion and kaon structures. In specific kinematic regions, an electron scattering process coupled with the observation of recoil nucleons (N) or hyperons (Y) receiving sufficiently low four-momentum transfer, $-t$, can reveal features associated with the 'meson cloud' of the nucleon. With a proper theoretical understanding of the interpretation of the off-shell pion (kaon) target and possible theoretical backgrounds as a function of $-t$, experimental access to a physical pion (kaon) target is enabled. This can be further experimentally validated by constraining the theoretical backgrounds using both ep and ed scattering data, and by ensuring an interpretation independent of $-t$. Based on current theoretical and experimental guidance, this may be possible for $-t < 0.6\,(0.9)\,\mathrm{GeV}^2$ for pion (kaon) targets. For elastic scattering, this Sullivan process carries information on the pion or kaon form factor. For DIS, the process informs us about the mesonic parton content. Regardless of interpretation, the various tagged pion (kaon) cross-section data as a function of $-t$ are valuable in their own right.

Since only a small fraction of the nucleons emit a virtual meson and only small momentum transfers from the nucleon to the resulting baryon allow the interpretation in terms of a real pion (kaon), the highest luminosities of $\sim 10^{34}$ electron–nucleons $\mathrm{cm}^{-2}\ \mathrm{s}^{-1}$ are necessary. Owing to the long lifetime of the $\Lambda$, lower collision (or rather proton/ion beam) energies are slightly favoured at the EIC to tag kaon structure. The need to efficiently tag pion and kaon structures is further fundamentally intertwined with the integration of the EIC detector in the interaction region, and in particular, related to any far-forward (in the direction of the proton/ion beam) detection scheme for recoil nucleons and hyperons. All sub-components of the far-forward area play an important role in the detection of forward-going protons (in Roman pots) and neutrons (in ZDCs), and the detection of hyperon decay products: protons and negatively charged pions at opposite sides of the beamline, and neutrons and photons originating from neutral pion decays in the zero-degree and electromagnetic calorimeters. It has been shown that appreciable detection efficiencies are thus achieved, with exception of kaon tagging at the highest EIC proton beam energies (275 GeV). The kaon tagging scheme could be improved by an alternate magneto-optic design, removing a large area with nearby and therefore integrated magnets in the present beamline, and hence no possible detection of decay products, or alternatively, an improved secondary focus.

This detection scheme allows, through the Sullivan process, excellent prospects for pion (and kaon) structural function measurements over a large range of $x$ and $Q^2$, approaching the vast $(x, Q^2)$ landscape of the HERA proton structural function measurements. The tagged pion (kaon) cross-section data remain precise over a large range of $-t$, up to $-t \sim 0.6\ \mathrm{GeV}^2$ for the pion. This could allow further study of more exclusive semi-inclusive and deeply-virtual Compton scattering data, towards transverse momentum and pressure distributions in the pion.

To access the pion form factor, an alternate technique is used to access the longitudinal cross-section, via a model validated with exclusive $\pi^+/\pi^-$ ratios from deuterium. Scattering from the pion cloud dominates the longitudinal cross-section at low $-t$, and, if dominant, this ratio would approach unity. This could allow precise pion form-factor determination at EIC at up to $Q^2 \sim 35$ GeV$^2$. The reliability of a similar $\Lambda/\Sigma$ ratio method for extracting the kaon form factor has not yet been established, but it may be studied using a Jefferson Lab 12 GeV kaon electroproduction experiment that ran in 2018/2019.

The EIC will play a key role in accessing pion and kaon structures over a wide range of CM energies, $\sim$2–140 GeV, to chart in-pion and in-kaon distributions of mass, charge, magnetisation, and perhaps angular momentum. Nonetheless, to provide experimental measurements that guide theoretical understanding requires a coherent, worldwide effort. Jefferson Lab will provide, at its CM energy $\sim$ 5 GeV, data for the pion (kaon) form factor up to $Q^2 \sim 10(5)$ GeV$^2$ and for insights into mechanisms competing with the Sullivan process, and early measurements of the pion (kaon) structural functions at large-$x$ ($>$0.5). AMBER can provide pion and, in particular, much-needed kaonic, Drell–Yan measurements in the CM energy region $\sim$ 10–20 GeV. These measurements are critical elements in a global effort to support pion and kaon structural function measurements. They also allow an independent determination of the ‘pion flux’ for EIC Sullivan process measurements. An EicC is under consideration, with a CM energy of $\sim$ 10–20 GeV that is perfectly attuned to AMBER and which would form a bridge from Jefferson Lab to EIC.

Successful completion of the programme sketched herein will deliver deep, far-reaching insights into the distributions and apportionment of charge, mass, and spin within the pion and kaon; the similarities and differences between such distributions in these (almost) NG modes and the benchmark proton; the symbiotic relationship between the emergence of hadron mass and confinement; and the character and consequences of constructive interference between the Standard Model’s two mass-generating mechanisms. It has the potential to finally complete a chapter in science whose first lines were written more than eighty years ago, and contained the prediction of the pion’s existence [201].

## Acknowledgments

This work was supported in part by the U.S. Department of Energy, Office of Science, Office of Nuclear Physics, under contracts DE-AC05-06OR23177, DE-FG02-03ER41260; the US National Science Foundation under Grants PHY-1653405, PHY-1714133, PHY-2012430; The Natural Sciences and Engineering Research Council of Canada (NSERC), FRN: SAPIN-2016-00031; the Jiangsu Province *Hundred Talents Plan for Professionals*; Ministerio Español de Ciencia e Innovación, Grant No. PID2019-107844GB-C22; Junta de Andalucía, Contract No. P18-FRJ-1132; Operativo FEDER Andalucía 2014–2020 UHU-1264517; Conselho Nacional de Desenvolvimento Científico e Tecnológico (CNPq) under Grant No. 308486/2015-3; Fundação de Amparo à Pesquisa do Estado de São Paulo (FAPESP) under the thematic project Grant 2017/05660-0; INCT-FNA project 464898/2014-5; Coordenação de Aperfeiçoamento de Pessoal de Nível Superior (CAPES—Finance Code 001); Research Corporation for Science Advancement through the Cottrell Scholar Award. The work of NS was supported by the DOE, Office of Science, Office of Nuclear Physics in the Early Career Programme. Contributions of and discussions with Wally Melnitchouk are gratefully acknowledged. The authors would like to thank Wim Cosyn and Doug Higinbotham for helpful comments during this work and preparation of this manuscript. The authors would also like to thank Zafar Ahmed, Rory Evans and Wenliang (Bill) Li for their work and assistance on the DEMP event generator.

## Data availability statement

The data that support the findings of this study are available upon reasonable request from the authors.

## ORCID iDs

J Arrington https://orcid.org/0000-0002-0702-1328
C Ayerbe Gayoso https://orcid.org/0000-0001-8640-5380
P C Barry https://orcid.org/0000-0001-6933-9166
V Berdnikov https://orcid.org/0000-0003-4916-6194
D Binosi https://orcid.org/0000-0003-1742-4689
L Chang https://orcid.org/0000-0002-4339-2943
M Diefenthaler https://orcid.org/0000-0002-4717-4484
M Ding https://orcid.org/0000-0002-3690-1690
R Ent https://orcid.org/0000-0001-7015-2534
T Frederico https://orcid.org/0000-0002-5497-5490
Y Furletova https://orcid.org/0000-0001-9032-1999
T J Hobbs https://orcid.org/0000-0002-2729-0015
T Horn https://orcid.org/0000-0003-1925-9541
G M Huber https://orcid.org/0000-0002-5658-1065
S J D Kay https://orcid.org/0000-0002-8855-3034
C Keppel https://orcid.org/0000-0002-7516-8292
H-W Lin https://orcid.org/0000-0002-0899-3866
C Mezrag https://orcid.org/0000-0001-8678-4085
R Montgomery https://orcid.org/0000-0002-2007-6833
I L Pegg https://orcid.org/0000-0002-1195-3013
K Raya https://orcid.org/0000-0001-8225-5821
P Reimer https://orcid.org/0000-0002-0301-2176
C D Roberts https://orcid.org/0000-0002-2937-1361
J Rodríguez-Quintero https://orcid.org/0000-0002-1651-5717
D Romanov https://orcid.org/0000-0001-6826-2291
G Salmè https://orcid.org/0000-0002-9209-3464
N Sato https://orcid.org/0000-0002-1535-6208
J Segovia https://orcid.org/0000-0001-5838-7103
P Stepanov https://orcid.org/0000-0002-0806-1743
A S Tadepalli https://orcid.org/0000-0002-5312-8943
R L Trotta https://orcid.org/0000-0002-8193-6139

## References

[1] Higgs P W 1964 Broken symmetries and the masses of gauge bosons *Phys. Rev. Lett.* **13** 508–9
[2] Aad G *et al* 2012 Observation of a new particle in the search for the Standard Model Higgs boson with the ATLAS detector at the LHC *Phys. Lett.* B **716** 1–29
[3] Chatrchyan S *et al* 2012 Observation of a new boson at a mass of 125 GeV with the CMS experiment at the LHC *Phys. Lett.* B **716** 30–61
[4] Roberts C D and Schmidt S M 2020 Reflections upon the emergence of hadronic mass *Eur. Phys. J. Spec. Top.* **229** 3319–40
[5] Roberts C D 2020 Empirical consequences of emergent mass *Symmetry* **12** 1468

[6] Roberts C D 2021 On mass and matter (arXiv:2101.08340 [hep-ph])
[7] Pascual P and Tarrach R 1984 *QCD: Renormalization for the Practitioner* (*Lecture Notes in Physics* vol 194) (Berlin: Springer)
[8] de Elvira J R, Hoferichter M, Kubis B and Meißner U-G 2018 Extracting the $\sigma$-term from low-energy pion–nucleon scattering *J. Phys. G: Nucl. Part. Phys.* **45** 024001
[9] Zyla P A *et al* 2020 Review of particle properties *Prog. Theor. Exp. Phys.* **2020** 083C01
[10] Nambu Y 1960 Quasi-particles and gauge invariance in the theory of superconductivity *Phys. Rev.* **117** 648–63
[11] Goldstone J 1961 Field theories with 'superconductor' solutions *Nuovo Cimento* **19** 154–64
[12] Ji X 1995 Breakup of hadron masses and the energy–momentum tensor of QCD *Phys. Rev.* D **52** 271–81
[13] Aguilar A C *et al* 2019 Pion and kaon structure at the electron–ion collider *Eur. Phys. J.* A **55** 190
[14] Brodsky S J *et al* 2020 Strong QCD from hadron structure experiments *Int. J. Mod. Phys.* E **29** 2030006
[15] Feder T 2020 Brookhaven facility to be transformed into electron–ion collider *Phys. Today* **73** 22
[16] Lattes C M G, Muirhead H, Occhialini G P S and Powell C F 1947 Processes involving charged mesons *Nature* **159** 694–7
[17] Rochester G D and Butler C C 1947 Evidence for the existence of new unstable elementary particles *Nature* **160** 855–7
[18] Roberts C D, Richards D G, Horn T and Chang L 2021 Insights into the emergence of mass from studies of pion and kaon structure (arXiv:2102.01765 [hep-ph])
[19] Peter Lepage G and Brodsky S J 1979 Exclusive processes in quantum chromodynamics: evolution equations for hadronic wavefunctions and the form factors of mesons *Phys. Lett.* B **87** 359–65
[20] Efremov A V and Radyushkin A V 1980 Factorization and asymptotic behaviour of pion form factor in QCD *Phys. Lett.* B **94** 245–50
[21] Farrar G R and Jackson D R 1979 Pion form factor *Phys. Rev. Lett.* **43** 246
[22] Lepage G P and Brodsky S J 1980 Exclusive processes in perturbative quantum chromodynamics *Phys. Rev.* D **22** 2157
[23] Roberts C D 2016 Three lectures on hadron physics *J. Phys.: Conf. Ser.* **706** 022003
[24] Horn T and Roberts C D 2016 The pion: an enigma within the Standard Model *J. Phys. G: Nucl. Part. Phys.* **43** 073001
[25] Eichmann G, Sanchis-Alepuz H, Williams R, Alkofer R and Fischer C S 2016 Baryons as relativistic three-quark bound states *Prog. Part. Nucl. Phys.* **91** 1–100
[26] Burkert V D and Roberts C D 2019 Roper resonance: toward a solution to the fifty year puzzle *Rev. Mod. Phys.* **91** 011003
[27] Qin S-X and Roberts C D 2020 Impressions of the continuum bound state problem in QCD *Chin. Phys. Lett.* **37** 121201
[28] Sales J H O, Frederico T, Carlson B V and Sauer P U 2000 Light front Bethe–Salpeter equation *Phys. Rev.* C **61** 044003
[29] Frederico T, Pace E, Pasquini B and Salme G 2009 Pion generalized parton distributions with covariant and light-front constituent quark models *Phys. Rev.* D **80** 054021
[30] Carbonell J and Karmanov V A 2010 Solving the Bethe–Salpeter equation for two fermions in Minkowski space *Eur. Phys. J.* A **46** 387–97
[31] Salmè G, Frederico T and Viviani M 2014 Solutions of the Bethe–Salpeter equation in Minkowski space: a comparative study *Few-Body Syst.* **55** 693–6
[32] Salmè G 2014 Investigating the homogeneous Bethe–Salpeter equation in Minkowski space *J. Phys.: Conf. Ser.* **527** 012026
[33] de Paula W, Frederico T, Salmè G and Viviani M 2016 Advances in solving the two-fermion homogeneous Bethe–Salpeter equation in Minkowski space *Phys. Rev.* D **94** 071901
[34] Chang L, Cloet I C, Cobos-Martinez J J, Roberts C D, Schmidt S M and Tandy P C 2013 Imaging dynamical chiral symmetry breaking: pion wave function on the light front *Phys. Rev. Lett.* **110** 132001
[35] 't Hooft G 1974 A two-dimensional model for mesons *Nucl. Phys.* B **75** 461–70
[36] Chang L, Cloet I C, Roberts C D, Schmidt S M and Tandy P C 2013 Pion electromagnetic form factor at spacelike momenta *Phys. Rev. Lett.* **111** 141802
[37] Chen M, Ding M, Chang L and Roberts C D 2018 Mass-dependence of pseudoscalar meson elastic form factors *Phys. Rev.* D **98** 091505

[38] Gao F, Chang L, Liu Y-X, Roberts C D and Tandy P C 2017 Exposing strangeness: projections for kaon electromagnetic form factors *Phys. Rev.* D **96** 034024

[39] Horn T *et al* 2008 Scaling study of the pion electroproduction cross sections and the pion form factor *Phys. Rev.* C **78** 058201

[40] Huber G M *et al* 2008 Charged pion form-factor between $Q^2 = 0.60$ GeV$^2$ and 2.45 GeV$^2$: II. Determination of, and results for, the pion form-factor *Phys. Rev.* C **78** 045203

[41] Huber G M, Gaskell D *et al* 2006 Measurement of the charged pion form factor to high $Q^2$ *Jefferson Lab Experiment E12-06-101*

[42] Horn T, Huber G M *et al* 2007 Scaling study of the L/T-separated pion electroproduction cross section at 11 GeV *Jefferson Lab 12 GeV Experiment E12-07-105*

[43] Horn T, Huber G M, Markowitz P *et al* 2009 Studies of the L/T separated kaon electroproduction cross sections from 5–11 GeV *Jefferson Lab 12 GeV Experiment E12-09-011*

[44] Qin S-X, Chen C, Mezrag C and Roberts C D 2018 Off-shell persistence of composite pions and kaons *Phys. Rev.* C **97** 015203

[45] Choi H-M, Frederico T, Ji C-R and de Melo J P B C 2019 Pion off-shell electromagnetic form factors: data extraction and model analysis *Phys. Rev.* D **100** 116020

[46] Keith Ellis R, James Stirling W and Webber B R 2011 *QCD and Collider Physics* vol 8 (Cambridge: Cambridge University Press) p 2

[47] Lane K 1974 Asymptotic freedom and Goldstone realization of chiral symmetry *Phys. Rev.* D **10** 2605

[48] Politzer H D 1976 Effective quark masses in the chiral limit *Nucl. Phys.* B **117** 397

[49] Maris P, Roberts C D and Tandy P C 1998 Pion mass and decay constant *Phys. Lett.* B **420** 267–73

[50] Ezawa Z F 1974 Wide-angle scattering in softened field theory *Nuovo Cimento* A **23** 271–90

[51] Farrar G R and Jackson D R 1975 Pion and nucleon structure functions near $x = 1$ *Phys. Rev. Lett.* **35** 1416

[52] Berger E L and Brodsky S J 1979 Quark structure functions of mesons and the Drell–Yan process *Phys. Rev. Lett.* **42** 940–4

[53] Brodsky S J, Burkardt M and Schmidt I 1995 QCD constraints on the shape of polarized quark and gluon distributions *Nucl. Phys.* B **441** 197–214

[54] Yuan F 2004 Generalized parton distributions at $x \to 1$ *Phys. Rev.* D **69** 051501

[55] Dokshitzer Y L 1977 Calculation of the structure functions for seep inelastic scattering and $e^+e^-$ annihilation by perturbation theory in quantum chromodynamics *Sov. Phys. - JETP* **46** 641–53

[56] Gribov V N and Lipatov L N 1971 Deep inelastic electron scattering in perturbation theory *Phys. Lett.* B **37** 78–80

[57] Lipatov L N 1975 The parton model and perturbation theory *Sov. J. Nucl. Phys.* **20** 94–102

[58] Altarelli G and Parisi G 1977 Asymptotic freedom in parton language *Nucl. Phys.* B **126** 298–318

[59] Ball R D, Nocera E R and Rojo J 2016 The asymptotic behaviour of parton distributions at small and large $x$ *Eur. Phys. J.* C **76** 383

[60] Drell S D and Yan T-M 1970 Connection of elastic electromagnetic nucleon form factors at large $Q^2$ and deep inelastic structure functions near threshold *Phys. Rev. Lett.* **24** 181–6

[61] West G B 1970 Phenomenological model for the electromagnetic structure of the proton *Phys. Rev. Lett.* **24** 1206–9

[62] Ezawa Z F 1973 Drell–Yan–West relation for deep-inelastic and elastic form factors *Nucl. Phys.* B **58** 295–300

[63] Landshoff P V and Polkinghorne J C 1973 Threshold properties of electroproduction and annihilation *Nucl. Phys.* B **53** 473–83

[64] Badier J *et al* 1983 Experimental determination of the pi meson structure functions by the Drell–Yan mechanism *Z. Phys.* C **18** 281

[65] Conway J S *et al* 1989 Experimental study of muon pairs produced by 252 GeV pions on tungsten *Phys. Rev.* D **39** 92–122

[66] Barry P C, Sato N, Melnitchouk W and Ji C-R 2018 First Monte Carlo global QCD analysis of pion parton distributions *Phys. Rev. Lett.* **121** 152001

[67] Novikov I *et al* 2020 Parton distribution functions of the charged pion within the xFitter framework *Phys. Rev.* D **102** 014040

[68] Han C, Xie G, Wang R and Chen X 2020 An analysis of parton distribution functions of the pion and the kaon with the maximum entropy input (arXiv:2010.14284)

[69] Aicher M, Schafer A and Vogelsang W 2010 Soft-gluon resummation and the valence parton distribution function of the pion *Phys. Rev. Lett.* **105** 252003

[70] Barry P C, Ji C-R, Melnitchouk W and Sato N Threshold resummation effects on pion PDFs at large *x* (in preparation).

[71] Cui Z-F, Ding M, Gao F, Binosi D, Chang L, Roberts C, Rodríguez-Quintero J and Schmidt S 2021 Higgs modulation of emergent mass as revealed in kaon and pion parton distributions *Eur. Phys. J.* A **57** 5

[72] Cui Z-F, Ding M, Gao F, Raya K, Binosi D, Chang L, Roberts C D, Rodríguez-Quintero J and Schmidt S 2020 Kaon and pion parton distributions *Eur. Phys. J.* C **80** 1064

[73] Sabbir Sufian R, Karpie J, Egerer C, Orginos K, Qiu J-W and Richards D G 2019 Pion valence quark distribution from matrix element calculated in lattice QCD *Phys. Rev.* D **99** 074507

[74] Zhang J-H, Chen J-W, Jin L, Lin H-W, Schäfer A and Zhao Y 2019 First direct lattice-QCD calculation of the *x*-dependence of the pion parton distribution function *Phys. Rev.* D **100** 034505

[75] Hecht M B, Roberts C D and Schmidt S M 2001 Valence quark distributions in the pion *Phys. Rev.* C **63** 025213

[76] Lin H-W, Chen J-W, Fan Z, Zhang J-H and Zhang R 2021 The valence-quark distribution of the kaon from lattice QCD *Phys. Rev.* D **103** 014516

[77] Badier J *et al* 1980 Measurement of the structure function ratio using the Drell–Yan process *Phys. Lett.* B **93** 354–6

[78] Ding M, Raya K, Binosi D, Chang L, Roberts C D and Schmidt S M 2020 Drawing insights from pion parton distributions *Chin. Phys.* C **44** 031002

[79] Ding M, Raya K, Binosi D, Chang L, Roberts C D and Schmidt S M 2020 Symmetry, symmetry breaking, and pion parton distributions *Phys. Rev.* D **101** 054014

[80] de Paula W, Ydrefors E, Alvarenga Nogueira J, Frederico T and Salmè G 2020 The pion valence momentum distributions and 3D image with Minkowski space dynamics (in preparation)

[81] Zhang J-L, Cui Z-F, Ping J and Roberts C D 2021 Contact interaction analysis of pion GTMDs *Eur. Phys. J.* C **81** 6

[82] Brömmel D *et al* 2008 The spin structure of the pion *Phys. Rev. Lett.* **101** 122001

[83] Nam S-i and Kim H-C 2011 Spin structure of the pion from the instanton vacuum *Phys. Lett.* B **700** 305–12

[84] Dorokhov A E, Broniowski W and Ruiz Arriola E 2011 Generalized quark transversity distribution of the pion in chiral quark models *Phys. Rev.* D **84** 074015

[85] Fanelli C, Pace E, Romanelli G, Salme G and Salmistraro M 2016 Pion generalized parton distributions within a fully covariant constituent quark model *Eur. Phys. J.* C **76** 253

[86] Zhang J-L, Raya K, Chang L, Cui Z-F, Morgado J M, Roberts C D and Rodríguez-Quintero J 2021 Measures of pion and kaon structure from generalised parton distributions (arXiv:2101.12286 [hep-ph])

[87] Wilson K G 1974 Confinement of quarks *Phys. Rev.* D **10** 2445–59

[88] Liu K-F and Dong S-J 1994 Origin of difference between anti-d and anti-u partons in the nucleon *Phys. Rev. Lett.* **72** 1790–3

[89] Liu K F, Dong S J, Draper T, Leinweber D, Sloan J H, Wilcox W, Woloshyn R M and Valence Q C D 1999 Connecting QCD to the quark model *Phys. Rev.* D **59** 112001

[90] Liu K-F 2000 Parton degrees of freedom from the path integral formalism *Phys. Rev.* D **62** 074501

[91] Detmold W and David Lin C J 2006 Deep-inelastic scattering and the operator product expansion in lattice QCD *Phys. Rev.* D **73** 014501

[92] Braun V M and Müller D 2008 Exclusive processes in position space and the pion distribution amplitude *Eur. Phys. J.* C **55** 349–61

[93] Ji X 2013 Parton physics on a Euclidean lattice *Phys. Rev. Lett.* **110** 262002

[94] Ji X 2014 Parton physics from large-momentum effective field theory *Sci. China Phys. Mech. Astron.* **57** 1407–12

[95] Ji X, Liu Y-S, Liu Y, Zhang J-H and Zhao Y 2020 Large-momentum effective theory (arXiv:2004.03543 [hep-ph])

[96] Radyushkin A V 2017 Nonperturbative evolution of parton quasi-distributions *Phys. Lett.* B **767** 314–20

[97] Chambers A J *et al* 2017 Nucleon structure functions from operator product expansion on the lattice *Phys. Rev. Lett.* **118** 242001

[98] Ma Y-Q and Qiu J-W 2018 Extracting parton distribution functions from lattice QCD calculations *Phys. Rev.* D **98** 074021

[99] Ma Y-Q and Qiu J-W 2015 QCD factorization and PDFs from lattice QCD calculation *Int. J. Mod. Phys. Conf. Ser.* **37** 1560041

[100] Ma Y-Q and Qiu J-W 2018 Exploring partonic structure of hadrons using *ab initio* lattice QCD calculations *Phys. Rev. Lett.* **120** 022003

[101] Lin H-W *et al* 2018 Parton distributions and lattice QCD calculations: a community white paper *Prog. Part. Nucl. Phys.* **100** 107–60

[102] Cichy K and Constantinou M 2019 A guide to light-cone PDFs from lattice QCD: an overview of approaches, techniques and results *Adv. High Energy Phys.* **2019** 3036904

[103] Zhang R, Honkala C, Lin H-W and Chen J-W 2020 Pion and kaon distribution amplitudes in the continuum limit *Phys. Rev.* D **102** 094519

[104] Bali G S *et al* 2018 Pion distribution amplitude from Euclidean correlation functions *Eur. Phys. J.* C **78** 217

[105] Bali G S *et al* 2018 Pion distribution amplitude from Euclidean correlation functions: exploring universality and higher-twist effects *Phys. Rev.* D **98** 094507

[106] Roberts C D 2019 Insights into the origin of mass *27th Int. Nuclear Physics Conf.* vol 9

[107] Izubuchi T, Jin L, Kallidonis C, Karthik N, Mukherjee S, Petreczky P, Shugert C and Syritsyn S 2019 Valence parton distribution function of pion from fine lattice *Phys. Rev.* D **100** 034516

[108] Joó B, Karpie J, Orginos K, Radyushkin A V, Richards D G, Sufian R S and Zafeiropoulos S 2019 Pion valence structure from Ioffe-time parton pseudodistribution functions *Phys. Rev.* D **100** 114512

[109] Sufian R S, Egerer C, Karpie J, Edwards R G, Joó B, Ma Y-Q, Orginos K, Qiu J-W and Richards D G 2020 Pion valence quark distribution from current−current correlation in lattice QCD *Phys. Rev.* D **102** 054508

[110] Chen J-W, Lin H-W and Zhang J-H 2020 Pion generalized parton distribution from lattice QCD *Nucl. Phys.* B **952** 114940

[111] Fan Z-Y, Yang Y-B, Anthony A, Lin H-W and Liu K-F 2018 Gluon quasi-parton-distribution functions from lattice QCD *Phys. Rev. Lett.* **121** 242001

[112] Balitsky I, Morris W and Radyushkin A 2020 Gluon pseudo-distributions at short distances: forward case *Phys. Lett.* B **808** 135621

[113] Wang W, Zhang J-H, Zhao S and Zhu R 2019 Complete matching for quasidistribution functions in large momentum effective theory *Phys. Rev.* D **100** 074509

[114] Zhang J-H, Ji X, Schäfer A, Wang W and Zhao S 2019 Accessing gluon parton distributions in large momentum effective theory *Phys. Rev. Lett.* **122** 142001

[115] Fan Z, Zhang R and Lin H-W 2020 Nucleon gluon distribution function from $2 + 1 + 1$-flavor lattice QCD (arXiv:2007.16113 [hep-lat])

[116] Burkardt M 2003 Impact parameter space interpretation for generalized parton distributions *Int. J. Mod. Phys.* A **18** 173–207

[117] Diehl M 2003 Generalized parton distributions *Phys. Rep.* **388** 41–277

[118] Collins J C, Soper D E and Sterman G 1989 Factorization of Hard Processes in QCD *Adv.Ser.Direct.High Energy Phys.* **5** 1–91

[119] Owens J F 1984 $Q^2$-dependent parametrizations of pion parton distribution functions *Phys. Rev.* D **30** 943

[120] Aurenche P, Baier R, Fontannaz M, Kienzle-Focacci M N and Werlen M 1989 The gluon content of the pion from high-$p_T$ photon production *Phys. Lett.* B **233** 517–21

[121] Sutton P J, Martin A D, Roberts R G and Stirling W J 1992 Parton distributions for the pion extracted from Drell–Yan and prompt photon experiments *Phys. Rev.* D **45** 2349–59

[122] Glück M, Reya E and Vogt A 1992 Pionic parton distributions *Z. Phys.* C **53** 651–5

[123] Glück M, Reya E and Schienbein I 1999 Pionic parton distributions revisited *Eur. Phys. J.* C **10** 313–7

[124] Wijesooriya K, Reimer P E and Holt R J 2005 The pion parton distribution function in the valence region *Phys. Rev.* C **72** 065203

[125] Betev B *et al* 1985 Differential cross-section of high mass muon pairs produced by a 194 GeV/c $\pi^-$ beam on a tungsten target *Z. Phys.* C **28** 9

[126] Chekanov S *et al* 2002 Leading neutron production in $e^+p$ collisions at HERA *Nucl. Phys.* B **637** 3–56

[127] Aaron F D *et al* 2010 Measurement of leading neutron production in deep-inelastic scattering at HERA *Eur. Phys. J.* C **68** 381–99

[128] McKenney J R, Sato N, Melnitchouk W and Ji C-R 2016 Pion structure function from leading neutron electroproduction and SU(2) flavor asymmetry *Phys. Rev.* D **93** 054011

[129] Holt R J and Roberts C D 2010 Nucleon and pion distribution functions in the valence region *Rev. Mod. Phys.* **82** 2991–3044

[130] Noguera S and Scopetta S 2015 Pion transverse momentum dependent parton distributions in the nambu and Jona–Lasinio model *J. High Energy Phys.* JHEP11(2015)102

[131] Hutauruk P T P, Cloet I C and Thomas A W 2016 Flavor dependence of the pion and kaon form factors and parton distribution functions *Phys. Rev.* C **94** 035201

[132] Hobbs T J 2018 Quantifying finite-momentum effects in the quark quasidistribution functions of mesons *Phys. Rev.* D **97** 054028

[133] Xu S-S, Chang L, Roberts C D and Zong H-S 2018 Pion and kaon valence-quark parton quasidistributions *Phys. Rev.* D **97** 094014

[134] Lan J, Mondal C, Jia S, Zhao X and Vary J P 2019 Parton distribution functions from a light front Hamiltonian and QCD evolution for light mesons *Phys. Rev. Lett.* **122** 172001

[135] Chang L, Raya K and Wang X 2020 Pion parton distribution function in light-front holographic QCD *Chin. Phys.* C **44** 114105

[136] Kock A, Liu Y and Zahed I 2020 Pion and kaon parton distributions in the QCD instanton vacuum *Phys. Rev.* D **102** 014039

[137] Aicher M, Schafer A and Werner V 2011 Threshold-resummed cross section for the Drell–Yan process in pion–nucleon collisions at COMPASS *Phys. Rev.* D **83** 114023

[138] Bonvini M, Marzani S, Rojo J, Rottoli L, Ubiali M, Ball R D, Bertone V, Carrazza S and Hartland N P 2015 Parton distributions with threshold resummation *J. High Energy Phys.* JHEP09(2015)191

[139] Westmark D and Owens J F 2017 Enhanced threshold resummation formalism for lepton pair production and its effects in the determination of parton distribution functions *Phys. Rev.* D **95** 056024

[140] Vogelsang W 2020 Soft-gluon resummation and the pion parton distribution function 06.02-05 *CFNS Workshop Series: Pion and Kaon Structure Functions at the EIC*

[141] Adikaram D *et al* 2015 Measurement of tagged deep inelastic scattering (TDIS) *Jefferson Lab Experiment E12-15-006*

[142] Hobbs T J 2015 Phenomenological implications of the nucleon's meson cloud *Few-Body Syst.* **56** 363–8

[143] Annand J *et al* 2015 Measurement of kaon structure function through tagged deep inelastic scattering (TDIS) *Jefferson Lab Experiment C12-15-006A*

[144] Cao N Y, Barry P C, Sato N and Melnitchouk W 2021 Towards the three-dimensional parton structure of the pion: integrating transverse momentum data into global QCD analysis (arXiv:2103.02159)

[145] Yang Y-B, Chen Y, Draper T, Gong M, Liu K-F, Liu Z and Ma J-P 2015 Meson mass decomposition from lattice QCD *Phys. Rev.* D **91** 074516

[146] Radyushkin A V 2017 Quasi-parton distribution functions, momentum distributions, and pseudo-parton distribution functions *Phys. Rev.* D **96** 034025

[147] Karpie J, Orginos K, Rothkopf A and Zafeiropoulos S 2019 Reconstructing parton distribution functions from Ioffe time data: from Bayesian methods to neural networks *J. High Energy Phys.* JHEP04(2019)057

[148] Del Debbio L, Giani T, Karpie J, Orginos K, Radyushkin A and Zafeiropoulos S 2020 Neural-network analysis of parton distribution functions from ioffe-time pseudodistributions (arXiv:2010.03996 [hep-ph])

[149] Constantinou M *et al* 2020 Parton distributions and lattice QCD calculations: toward 3D structure (arXiv:2006.08636 [hep-ph])

[150] Bringewatt J, Sato N, Melnitchouk W, Qiu J-W, Steffens F and Constantinou M 2021 Confronting lattice parton distributions with global QCD analysis *Phys. Rev.* D **103** 016003

[151] Lin H-W, Melnitchouk W, Prokudin A, Sato N and Shows H 2018 First Monte Carlo global analysis of nucleon transversity with lattice QCD constraints *Phys. Rev. Lett.* **120** 152502

[152] Alexandrou C, Cichy K, Constantinou M, Hadjiyiannakou K, Jansen K, Scapellato A and Steffens F 2020 Unpolarized and helicity generalized parton distributions of the proton within lattice QCD *Phys. Rev. Lett.* **125** 262001

[153] Lin H-W 2020 Nucleon tomography and generalized parton distribution at physical pion mass from lattice QCD (arXiv:2008.12474 [hep-ph])

[154] Radyushkin A V 2019 Generalized parton distributions and pseudodistributions *Phys. Rev.* D **100** 116011

[155] Hobbs T J, Wang B-T, Nadolsky P M and Olness F I 2019 Charting the coming synergy between lattice QCD and high-energy phenomenology *Phys. Rev.* D **100** 094040

[156] Kovařík K, Nadolsky P M and Soper D E 2020 Hadronic structure in high-energy collisions *Rev. Mod. Phys.* **92** 045003

[157] Dirac P A M 1949 Forms of relativistic dynamics *Rev. Mod. Phys.* **21** 392–9

[158] Miller G A and Brodsky S J 2020 Frame-independent spatial coordinate $\tilde{z}$: implications for light-front wave functions, deep inelastic scattering, light-front holography, and lattice QCD calculations *Phys. Rev.* C **102** 022201

[159] de Paula W, Ydrefors E, Alvarenga Nogueira J H, Frederico T and Salmè G 2021 Observing the minkowskian dynamics of the pion on the null-plane *Phys. Rev.* D **103** 014002

[160] de Melo J P B C, Sales J H O, Frederico T and Sauer P U 1998 Pairs in the light-front and covariance *Nucl. Phys.* A **631** 574–9

[161] Collins J 2018 The non-triviality of the vacuum in light-front quantization: an elementary treatment (arXiv:1801.03960)

[162] Chabysheva S S and Hiller J R 2020 Transitioning from equal-time to light-front quantization in $\phi_2^4$ theory *Phys. Rev.* D **102** 116010

[163] Martinovič L and Dorokhov A 2020 Vacuum loops in light-front field theory *Phys. Lett.* B **811** 135925

[164] Mannheim P D, Lowdon P and Brodsky S J 2020 Comparing light-front quantization with instant-time quantization 2005.00109

[165] Abdul Khalek R *et al* 2021 Science requirements and detector concepts for the electron-ion collider: EIC yellow report (arXiv:2103.05419)

[166] Sullivan J D 1972 One-pion exchange and deep-inelastic electron–nucleon scattering *Phys. Rev.* D **5** 1732–7

[167] Adloff C *et al* 1999 Measurement of leading proton and neutron production in deep inelastic scattering at HERA *Eur. Phys. J.* C **6** 587–602

[168] Kopeliovich B, Povh B and Potashnikova I 1996 Deep-inelastic electroproduction of neutrons in the proton fragmentation region *Z. Phys.* C **73** 125–31

[169] Nikolaev N N, Schafer W, Szczurek A and Speth J 1999 Do the E866 Drell–Yan data change our picture of the chiral structure of the nucleon? *Phys. Rev.* D **60** 014004

[170] Golec-Biernat K, Kwieciński J and Szczurek A 1997 Reggeon and pion contributions in semiexclusive diffractive processes at DESY HERA *Phys. Rev.* D **56** 3955–60

[171] Kazarinov Y M, Kopeliovich B Z, Lapidus L I and Potashnikova I K 1976 Triple regge phenomenology in the reaction $p + p \to p + \mathrm{X}$ *Sov. Phys. - JETP* **43** 598

[172] D'Alesio U and Pirner H J 2000 Target fragmentation in pp, ep and $\gamma$p collisions at high-energies *Eur. Phys. J.* A **7** 109–19

[173] Stoks V G J and Rijken T A 1999 Soft-core baryon–baryon potentials for the complete baryon octet *Phys. Rev.* C **59** 3009–20

[174] Hawker E A *et al* 1998 Measurement of the light anti-quark flavor asymmetry in the nucleon sea *Phys. Rev. Lett.* **80** 3715–8

[175] Adams B *et al* 2019 COMPASS++/AMBER: proposal for measurements at the M2 beam line of the CERN SPS phase-1: 2022–2024 *Technical Report CERN-SPSC-2019-022. SPSC-P-360, CERN, Geneva, May 2019* (The collaboration has not yet constituted itself, thus instead of a spokesperson currently the nominated contact person (Jan Friedrich) is acting in place)

[176] Chen X, Guo F-K, Roberts C D and Wang R 2020 Selected science opportunities for the EicC *Few-Body Syst.* **61** 43

[177] Trotta R 2020 EIC meson MC https://github.com/JeffersonLab/EIC_mesonMC/tree/master

[178] Volmer J *et al* 2001 Measurement of the charged pion electromagnetic form-factor *Phys. Rev. Lett.* **86** 1713–6

[179] Horn T *et al* 2006 Determination of the pion charge form factor at $Q^2 = 1.60$ and 2.45 $(\mathrm{GeV/c})^2$ *Phys. Rev. Lett.* **97** 192001

[180] Tadevosyan V *et al* 2007 Determination of the pion charge form factor for $Q^2 = 0.60$–1.60 GeV$^2$ *Phys. Rev.* C **75** 055205

[181] Blok H P *et al* 2008 Charged pion form factor between $Q^2 = 0.60$ and 2.45 GeV$^2$: I. Measurements of the cross section for the $^1\mathrm{H}(e, e'\pi^+)n$ reaction *Phys. Rev.* C **78** 045202

[182] Huber G M *et al* 2014 Separated response function ratios in exclusive, forward $\pi^\pm$ electroproduction *Phys. Rev. Lett.* **112** 182501

[183] Huber G M *et al* 2015 Separated response functions in exclusive, forward $\pi^\pm$ electroproduction on deuterium *Phys. Rev.* C **91** 015202

[184] Gluckstern R L 1963 Uncertainties in track momentum and direction, due to multiple scattering and measurement errors *Nucl. Instrum. Methods* **24** 381–9

[185] Vrancx T and Ryckebusch J 2014 Charged pion electroproduction above the resonance region *Phys. Rev.* C **89** 025203

[186] Amendolia S R *et al* 1984 A measurement of the pion charge radius *Phys. Lett.* B **146** 116–20

[187] Amendolia S R *et al* 1986 A measurement of the space-like pion electromagnetic form-factor *Nucl. Phys.* B **277** 168

[188] Ackermann H, Azemoon T, Gabriel W, Mertiens H D, Reich H D, Specht G, Janata F and Schmidt D 1978 Determination of the longitudinal and the transverse part in $\pi^+$ electroproduction *Nucl. Phys.* B **137** 294–300

[189] Brauel P, Canzler T, Cords D, Felst R, Grindhammer G, Helm M, Kollmann W-D, Krehbiel H and Schädlich M 1979 Electroproduction of $\pi^+n$, $\pi^-p$ and K$^+\Lambda$, K$^+$ 2211; 0 final states above the resonance region *Z. Phys.* C **3** 101

[190] Huber G M, Gaskell D, Horn T *et al* 2019 Measurement of the charged pion form factor to high $Q^2$ and scaling study of the L/T-separated pion electroproduction cross section at 11 GeV *Jefferson Lab 12 GeV Experiment E12-19-006*

[191] Melnitchouk W 2003 Quark-hadron duality in electron–pion scattering *Eur. Phys. J.* A **17** 223–34

[192] Nesterenko V A and Radyushkin A V 1982 Sum rules and the pion form factor in QCD *Phys. Lett.* B **115** 410

[193] Mello C S, de Melo J P B C and Frederico T 2017 Minkowski space pion model inspired by lattice QCD running quark mass *Phys. Lett.* B **766** 86–93

[194] Bakulev A P, Passek-Kumericki K, Schroers W and Stefanis N G 2004 Pion form-factor in QCD: from nonlocal condensates to NLO analytic perturbation theory *Phys. Rev.* D **70** 033014
Bakulev A P, Passek-Kumericki K, Schroers W and Stefanis N G 2004 *Phys. Rev.* D **70** 079906 (erratum)

[195] Choi T K, Kong K J and Yu B G 2015 Pion and proton form factors in the regge description of electroproduction $p(e, e'\pi^+)n$ *J. Korean Phys. Soc.* **67** 1089–94

[196] Carmignotto M *et al* 2018 Separated kaon electroproduction cross section and the kaon form factor from 6 GeV JLab data *Phys. Rev.* C **97** 025204

[197] Mohring R M *et al* 2003 Separation of the longitudinal and transverse cross sections in the $^1$H$(e, e'K^+)\Lambda$ and $^1$H$(e, e'K^+)\Sigma^0$ reactions *Phys. Rev.* C **67** 055205

[198] Coman M *et al* 2010 Cross sections and Rosenbluth separations in $^1$H$(e, e'K^+)\Lambda$ up to $Q^2 = 2.35$ GeV$^2$ *Phys. Rev.* C **81** 052201

[199] Oppenheimer J R *et al* 1957 Strange particles and weak interactions *7th Annual Rochester Conf. on High Energy Nuclear Physics* p IX.1–52

[200] Yamanaka T 2019 Detection of a strange particle *Nature* **575** 36–8

[201] Yukawa H 1935 On the interaction of elementary particles *Proc. Phys. Math. Soc. Japan* **17** 48–57